

Atomistic modeling of metal-nonmetal interphase boundary diffusion

I. Chesser¹, R. K. Koju¹, A. Vellore² and Y. Mishin¹

¹Department of Physics and Astronomy, MSN 3F3,
George Mason University, Fairfax, VA 22030, USA

²Thomas Jefferson High School for Science and Technology, Alexandria, VA 22312, USA

August 24, 2023

Atomistic computer simulations are applied to investigate the atomic structure, thermal stability, and diffusion processes in Al-Si interphase boundaries as a prototype of metal-ceramic interfaces in composite materials. Some of the most stable orientation relationships between the phases found in this work were previously observed in epitaxy experiments. A non-equilibrium interface can transform to a more stable state by a mechanism that we call interface-induced recrystallization. Diffusion of both Al and Si atoms in stable Al-Si interfaces is surprisingly slow compared with diffusion of both elements in Al grain boundaries but can be accelerated in the presence of interface disconnections. A qualitative explanation of the sluggish interphase boundary diffusion is proposed. Atomic mechanisms of interphase boundary diffusion are similar to those in metallic grain boundaries and are dominated by correlated atomic rearrangements in the form of strings and rings of collectively moving atoms.

Keywords: Atomistic modeling, diffusion, interphase boundary, grain boundary

1 Introduction

Metal-ceramic interfaces play an important role in many processes in structural and electronic materials [1–3]. In particular, they often control the mechanical behavior of metal-matrix composites reinforced with ceramic inclusions [3–12]. During the composite deformation at low and medium temperatures, the damage usually starts at matrix-reinforcer interfaces and accumulates by several concurrently operating mechanisms, including the interface shearing, debonding, and interaction with dislocations coming from the metallic

matrix. During creep deformation, the interface resistance to shear ensures that the re-inforcer carries much of the applied load, imparting a high creep resistance to the entire material [13–16]. However, at high enough temperatures, the interfaces lose much of their shear resistance and the load shifts back to the metallic matrix. As a result, the creep resistance decreases and can even fall below that of the matrix material [17].

The high-temperature sliding at metal-ceramic interfaces is not accompanied by interface debonding or any visible accumulation of damage. This process is fundamentally different from the low-temperature sliding friction and has been identified as a distinct physical phenomenon called interfacial creep [18–20]. Although the microscopic mechanisms of interfacial creep remain largely unknown, the process is clearly controlled by diffusive mass transport of the metallic elements along the metal-ceramic interface.

Much of the effort to understand the interfacial creep has focused on the binary Al-Si system as a simple model of a composite material. This system combines a soft metal with a hard covalent material representing the ceramic phase. The system features a simple eutectic phase diagram with low mutual solubility in the solid state, making it ideal for a fundamental study. Peterson et al. [20–22] studied interfacial creep at individual Al-Si interfaces using a single crystal of Si sandwiched between two polycrystalline Al layers. The interfacial creep rates measured at a series of loads and temperatures gave the activation energy of 42 kJ/mol, which is smaller than the experimental activation energy of Al grain boundary (GB) diffusion (84 kJ/mol). However, this result could not be interpreted unambiguously due to the highly non-equilibrium structure of the interfaces. High-resolution transmission electron microscopy (TEM) revealed a 20 nm thick amorphous interfacial layer stabilized by the oxygen coming from the native oxide layer on the Al surface. Attempts to gain insights into the diffusional creep at Al-Si interfaces were also made by other authors [19, 23, 24], but little progress has been made in understanding the underlying mechanisms.

A critical ingredient for studying the interfacial creep is the knowledge of interface diffusion coefficients. Unfortunately, while diffusion along metal-metal interphase boundaries has been measured in several systems [25–28], little is known about diffusion along metal-nonmetal interfaces. Qualitatively, it is well-recognized that interface diffusion is faster than lattice diffusion [26]. However, there is no consensus regarding the placement of metal-nonmetal interfaces relative to GB diffusion, surface diffusion, and diffusion in liquids. Experimental measurements of interphase boundary diffusion are extremely challenging. The only direct measurement known to us was for indium chemical diffusion along Sn-Ge twist interfaces [29]. Among indirect measurements, Kosinova et al. [30] back-calculated Au diffusion coefficients along Au-sapphire interfaces by comparing experimental observations of solid-state dewetting with a kinetic model of the process. The diffusion coefficients obtained were comparable with those for Au diffusion along non-singular surfaces. Kumar et al. [31] studied the kinetics of partial solid-state dewetting of a Ni film from a sapphire

substrate and estimated the Ni diffusivity along the Ni-Al₂O₃ interface. Their results, supported by first-principles density-functional theory (DFT) calculations, suggest that the rate of Ni diffusion along this interface is close to the rate of Ni self-diffusion in Ni GBs. On the other hand, Barda et al. [32] applied a similar experimental method and found that Au hetero-diffusion along the same Ni-Al₂O₃ interface was slower than Au hetero-diffusion in Ni GBs.

Specifically for Al-Si interphase boundaries, we are unaware of any direct or indirect diffusion measurements. The most accurate and direct diffusion measurements are made with radioactive isotopes. Unfortunately, Al does not have a suitable isotope for diffusion measurements [33]. The only suitable radioactive isotope of Si is ³¹Si, which has a short lifetime (2.6 hours). This drastically limits the time for diffusion experiments making them highly challenging [33]. Under the circumstances, atomistic computer simulations offer the only viable option for studying the interface diffusion in Al-Si. In addition to predicting diffusion coefficients, atomistic simulations can help discover the atomic-level mechanisms of the diffusion process.

Previous atomistic simulations of the Al-Si system were conducted at room temperature or 0 K. They additionally assumed that the interfaces were atomically sharp and separated pure Al from pure Si. It is well-established, however, that interfaces are more diffuse at high temperatures than at room temperature and separate solid solutions rather than pure elements. Furthermore, the previous simulations primarily targeted the cohesive strength and shear resistance of the interfaces, and the interface interactions with dislocations coming from the metallic side and absorbed by or transmitted through the interface [6, 34–39]. To our knowledge, no simulations have been performed for mass transport along Al-Si interphase boundaries. The most relevant simulation work has been published by Wu et al. [38], who calculated Al vacancy formation and migration energies at the Al (111) || Si (111) interface. The results suggest the possibility of faster interface diffusion relative to Al self-diffusion in the lattice, but no comparison with GB diffusion was discussed.

This paper reports on atomistic computer simulations of Al and Si diffusion along Al-Si interphase boundaries at relatively high temperatures up to the eutectic point. A significant part of this work was dedicated to constructing such boundaries with diverse orientation relationships between the phases and evaluating their structural stability during high-temperature anneals. The interface diffusion coefficients were extracted from direct molecular dynamics simulations without any adjustable parameters or model assumptions other than the approximations underlying the interatomic potential. To put our results in perspective, we also computed the diffusion coefficients of both elements in GBs and the bulk liquid phase. The collective nature of the interface diffusion mechanisms was investigated and compared with that in Al GB diffusion. In section 4, we propose a qualitative explanation of the sluggish interphase boundary diffusion in the Al-Si system found in this

work.

2 Methods

The Large-scale Atomic/Molecular Massively Parallel Simulator (LAMMPS) [40] was utilized to conduct Monte Carlo (MC) and molecular dynamics (MD) simulations. The software package OVITO [41] was used to visualize and analyze interface structures and diffusion mechanisms. A semi-empirical interatomic potential [42] was used to model interatomic bonding in the Al-Si system. This potential was made compatible with 2022 versions of LAMMPS as part of the publicly available lammeps-plugins package [43].

2.1 Phase diagram calculations

Simulations of the Al-Si interphase boundaries require the knowledge of the Al-Si phase diagram predicted by the interatomic potential. Experimentally, the Al-Si system has a simple eutectic phase diagram with a wide solid-solid miscibility gap and relatively small solubility limits in the terminal solid solutions. The Al-based and Si-based solutions have face-centered cubic (FCC) and diamond cubic (DC) crystalline structures, respectively. They will be referred to as simply Al and Si when no ambiguity can arise. Although the phase diagram predicted by this potential was previously computed [42] by a thermodynamic integration technique, we decided to verify the diagram by independent calculations using the phase coexistence method applied in prior work [44–47]. The solidus and liquidus lines on the phase diagram were computed by joining a solid layer and a liquid layer with periodic boundary conditions, so the system effectively contained two parallel solid-liquid interfaces. The initial phase compositions were chosen according to the phase diagram computed previously [42]. The system was subjected to a hybrid MC/MD anneal in which alternating blocks of MC swap attempts, and MD integration steps were performed in the isothermal-isobaric (NPT) ensemble at a set temperature. Swap attempts involved exchanges of chemical types of randomly selected pairs of Al and Si atoms and were accepted or rejected according to the Metropolis criterion. The approach to equilibrium was accompanied by solid-liquid interface motion and compositional changes in both phases. Equilibrium was achieved when the interfaces ceased to migrate and continued to fluctuate around constant positions while the bulk phase compositions reached steady-state values. The solidus and liquidus compositions were then calculated by averaging the compositions of bulk phase regions at least 2 nm away from the interfaces. To verify the system size convergence, multiple system sizes were tested both parallel and normal to the interface plane at several temperatures. Examples of convergence tests can be found in Supplementary Fig. 2. The results reported below are for a system containing around 20,000 atoms, the

interface cross-section of 2 nm by 2 nm, and the initial liquid and solid phase thicknesses of 20 nm each.

The solvus line calculations were performed using a similar solid-solid phase coexistence method. The known disadvantage of this approach is the low mobility of solid-solid interfaces. Nevertheless, convergence was achieved at several temperatures close to the eutectic temperature T_{eu} for a set of interfaces with sufficient mobility. Such interfaces exhibited a step flow migration mechanism in which Si atoms were added to existing Si steps at the interface. The interface migration distances observed were 0.5 nm or less. The solid-solid systems contained 5000 atoms with 6 nm thick Al and Si layers.

2.2 Interphase boundary construction and equilibration

Two methods were applied to create equilibrium interphase boundaries: the direct bonding method and the simulated epitaxy approach.

In the direct bonding method, unrelaxed interface structures were created by bonding Al and Si grains of specified crystallographic orientations along a planar interface with periodic boundary conditions parallel to the interface plane (X and Y coordinate axes) and free-surface boundary conditions normal to the interface (Z axis). Each grain had a thickness of at least 6 nm. Al and Si lattices exhibit a significant misfit with the 0 K ratio of the lattice parameters along the $\langle 100 \rangle$ direction equal to $a_{\text{Si}}/a_{\text{Al}} = 1.34$. The interface plane dimensions were chosen sufficiently large to ensure a 1% or smaller misfit strain along the X and Y directions. The misfit strain was applied homogeneously to the Al grain to meet periodic boundary conditions. This misfit strain varied slightly with temperature according to the precomputed thermal expansion coefficients of Al and Si at the temperature of simulations. Several smaller systems with larger misfit strains were studied in the context of the interface-induced recrystallization effect described below.

The interface structure was relaxed by hybrid MC/MD simulations to achieve structural and chemical equilibration. To this end, a fraction of randomly selected Al atoms were converted to Si atoms. This fraction was adjusted to match the estimated solid solubility of Si in Al along the solvus line on the computed Al-Si phase diagram at the chosen temperature. Next, an MC/MD anneal was performed with alternating blocks of MC swap attempts and MD integration steps in the canonical NVT ensemble. The number of swap attempts in each MC block was equal to twice the number of Al atoms in the system. The MD blocks were chosen to be 80 ps long, which was enough to sample atomic rearrangement events distinct from vibrations. Throughout the annealing procedure, a 1 nm slab containing the bottommost Si surface was frozen in place and excluded from dynamics. A 1 nm slab was also fixed at the top of the Al layer and excluded from dynamics (apart from the initial composition seed). This slab was allowed to float freely as a rigid body during the MD

steps to relieve pressure normal to the interface and accommodate possible spontaneous sliding events at the interface. Convergence of the MC/MD calculations was monitored by tracking the total potential energy of the system, the concentration of Si in the Al lattice, and the total number of disordered atoms at the interface that had neither FCC nor DC coordination. At high temperatures approaching the eutectic temperature, convergence was typically achieved after several ns of MD time and 10^6 MC swap attempts. Production runs were then performed for 20-40 ns and several million swap attempts.

The simulated epitaxy method was applied to find thermodynamically preferred interface orientation relationships as a function of the Si substrate orientation, temperature, and system size. The method permits a discovery of interfaces that are difficult to find by the direct bonding methodology, such as the interfaces with small lattice rotations away from high symmetry orientations.

As the starting point of the method, unrelaxed interfaces were created by the direct bonding method described above. The Al layer was then melted and re-solidified on top of the Si layer by the following multi-step procedure. First, the Al layer was separated from the Si layer by creating a 1 nm thick vacuum layer at the interface. The Si surface was then annealed for 0.1 ns at the set temperature, with all atoms of the Al layer held fixed. This step allowed for possible reconstruction on the Si surface. Next, the Al layer was quickly heated to 1200 K and held for 0.1 ns, with the Si layer excluded from dynamics. Since the melted Al layer was allowed to float in the normal direction, it closed the gap to wet the Si surface. The entire system was then quenched to a target temperature and annealed in the NVT ensemble for several ns using MD only. During the anneal, the Al layer solidified epitaxially on the Si surface. The epitaxial orientation relationship obtained was quantified using the grain segmentation and polyhedral template matching (PTM) modifiers in OVITO [48]. Selected epitaxial structures were subsequently annealed with an additional MC/MD run to examine the interface structure and verify the interface stability.

2.3 Grain boundary construction and equilibration

A set of Al and Si GBs was created to investigate GB diffusion. Unrelaxed single-component Al and Si GBs were constructed by joining two grains in a simulation box with periodic boundary conditions in the GB plane and free-surface boundary conditions normal to the GB. Supplementary Table 1 specifies the crystallography of each GB constructed. The GB cross-section had dimensions of at least 10 nm by 10 nm, and each grain had a thickness of at least 6 nm. A typical simulation box contained 50,000 to 100,000 atoms. For commensurate GBs, the lateral bicrystal dimensions were chosen with integer repeats of the coincident site lattice unit cell. For the incommensurate GB with the $\langle 100 \rangle$ and $\langle 110 \rangle$ directions parallel to the X axis, a small strain of approximately 1.001 was applied to the

upper grain to satisfy periodic boundary conditions.

The initial GB structures were optimized by a grid search that seeks to find a deep energy minimum. Several hundred initial unrelaxed GB structures were prepared with different rigid-body shifts applied to the upper grain relative to the lower. For each initial structure, pairs of closely spaced atoms were identified, and one atom was deleted at random if the overlap radius was in the range $(0.7-0.95)r_0$, where r_0 is the first nearest neighbor distance in FCC Al or DC Si. Conjugate-gradient energy minimization was then performed at 0 K to relax the GB core atoms in each candidate structure. The lowest-energy structure was used as input for the subsequent diffusion simulations. This optimization procedure recovered the well-known structures of the $\Sigma 3$ and $\Sigma 17$ GBs in Al and the $\Sigma 17$ GB in Si previously found with a Tersoff-type interatomic potential [49].

The lowest-energy GB structures were further equilibrated by a multi-step MD simulation in the NVT ensemble. First, the bicrystal was homogeneously expanded by the precomputed lattice thermal expansion strain at the chosen temperature. A 1 nm thick rigid slab at the top of the upper grain was allowed to float in the normal direction during a short (0.1 ns) NVT anneal. Combined with the pre-expansion, this step reduced the stresses in the grains to near zero. Next, the rigid-body slabs at the top and bottom of the bicrystal were fixed and an NVT anneal was performed for up to 20 ns. The fixed boundary conditions suppressed any spontaneous GB sliding events.

In addition to the elemental GBs, the $\Sigma 3$ and $\Sigma 17$ GB structures were created in Al-Si alloys with a bulk concentration of 8 at.% Si. The hybrid MC/MD method was employed for chemical and structural equilibration using the protocol described previously for the interphase boundaries. Convergence of Si GB segregation was achieved within several ns of MD time and approximately 10^6 MC swap attempts. Note that the alloy GBs represented a single-phase state and thus had an additional degree of freedom compared with the interphase boundaries. An alloy GB could be studied at any chemical composition and temperature within the Al-rich single-phase domain on the phase diagram. By contrast, only temperature could be varied for an interphase boundary while the phase compositions were uniquely defined by the solvus lines on the phase diagram.

2.4 Interface diffusion coefficient calculations

GB and interphase boundary self-diffusion coefficients were measured by tracking the motion Al and Si atoms within a 2 nm thick layer centered at the interface during the production MD runs in the microcanonical (NVE) ensemble which lasted between 1 ns and 40 ns. The interface position was determined as the average Z -coordinate of non-FCC and non-DC atoms identified by the PTM modifier in OVITO [48]. The diffusion coefficients in the interface layer were calculated from the Einstein relations $D_x = \langle x^2 \rangle / 2t$

and $D_y = \langle y^2 \rangle / 2t$, where $\langle x^2 \rangle$ and $\langle y^2 \rangle$ are the mean squared displacements (MSDs) of atoms in the in-plane X and Y directions and t is the simulation time. Bootstrap resampling was employed as in [50] to compute error estimates associated with the diffusion coefficients. The hyper-parameters chosen for this method included a smoothing window of 5 ps, a block length of 20 ps, and a number of resampled trajectories equal to 100. To mitigate the effect of lattice diffusion on the extracted interface diffusion coefficients, only atoms that remained in the calculation box at initial and final times were considered. The diffusion coefficients were additionally averaged over at least three independent runs with different initial composition and/or velocity seeds. For the interface containing disconnections, the diffusion coefficients were averaged over five initial velocity seeds.

Using a fixed-width layer underestimates the actual interface diffusion coefficient because of the inclusion of immobile atoms from the adjacent perfect lattice regions. For Al diffusion, this underestimation was corrected by rescaling the diffusion coefficients by the inverse fraction of perfectly coordinated FCC atoms averaged over the duration of the simulation. For Si diffusion, the diffusion coefficients were rescaled by the time-averaged inverse fraction of perfectly coordinated FCC and DC atoms. The latter rescaling relies on the observation that Si atoms occupy substitutional lattice positions in Al-Si alloys and are FCC-coordinated. Local coordination was determined with the PTM modifier [48] in OVITO with a cutoff value of 0.4.

2.5 Liquid diffusion coefficient calculations

To compute liquid diffusion coefficients, an initial 32,000-atom liquid structure was created in a periodic box by heating an Al crystal in the NPT ensemble to 1500 K and holding it for 200 ps. Next, a set of liquid samples was generated in the temperature range from 1050 to 1450 K by quenching the high-temperature structure at a rate of 50 K/100 ps and holding it at a set temperature for 200 ps. A further stepwise quenching was performed from 1050 K to 600 K at a rate of 25 K/ns with a hold time of 2 ns every 50 K. These times were sufficient for liquid equilibration at the chosen temperatures as evidenced by converged total potential energy and linear MSD vs time behavior.

An equivalent procedure was used for Al-Si eutectic liquid with 27 at.% Si and pure Si liquid. For pure Si, a larger initial melting temperature of 2000 K was employed. After obtaining well-equilibrated structures, production NVE anneals were performed for all liquid structures for 0.1 ns. The diffusivity was computed from the 3D Einstein relation $D = \langle r^2 \rangle / 6t$ and averaged over five independent runs with different velocity seeds. Crystallization was observed at sufficiently low temperatures. Diffusion data for such cases is not reported here.

2.6 Analysis of collective diffusion mechanisms

The following algorithm was used to identify correlated string-like clusters of mobile atoms during interface diffusion. First, mobile atoms were identified within the interphase boundary or GB such that the net displacement of an atom Δr during a time interval Δt was within the range $0.4r_0 < \Delta r < 1.2r_0$. Here, the upper bound was chosen to eliminate atoms that had undergone multiple hops, and the lower bound was chosen to eliminate immobile atoms. Next, mobile atomic pairs (i, j) were found that remained nearest neighbors at the times $t = 0$ and $t = \Delta t$ and satisfied the criterion $\min(|\mathbf{r}_i(t) - \mathbf{r}_j(0)|, |\mathbf{r}_j(t) - \mathbf{r}_i(0)|) < 0.43r_0$, where $\mathbf{r}_i(t)$ is the dynamic trajectory of atom i . This criterion identifies atomic pairs with string-like motion in which one atom jumps into the previous position of the other. The algorithm has three hyper-parameters: the lower and upper bounds for the displacement and the substitution distance (the factors 0.4, 1.2 and 0.43 above). These parameters were chosen based on the prior studies of diffusion in glass-forming supercooled liquids [51, 52] and were fixed across all interfaces studied in this work.

3 Results

3.1 Al-Si phase diagram

The Al-Si binary phase diagram computed in this work is shown in Supplementary Fig. 1. It is topologically similar to the experimental diagram [53] and differs quantitatively from the diagram computed by Saidi et al. [42] with the same interatomic potential. In particular, our calculations give a lower eutectic temperature T_{eu} and a higher Si concentration in the eutectic liquid than reported in [42]. We believe that our calculations are more accurate. The phase coexistence method implemented in this work is direct and more reliable than the thermodynamic integration method used in [42]. To further validate our calculations, we performed additional simulations involving phase changes. For example, we observed melting of solid-solid systems when they were heated above the eutectic temperature computed in this work but below T_{eu} reported in [42].

The phase diagram predicted by this potential overestimates the maximum solid solubility of Si in Al (0.12 ± 0.01 Si mole fraction) compared with experiment (0.015) [53]. It also overestimates the experimental eutectic composition (0.27 ± 0.02 versus 0.122). Furthermore, although the Al and Si melting temperatures are reproduced fairly accurately, the computed eutectic temperature (675 ± 5 K) is lower than the experimental value (850 K) [53]. Other interatomic potentials for the Al-Si system [54, 55] report even lower T_{eu} values. Thus, while the interatomic potential used in this work captures the correct topology of the Al-Si phase diagram and has certain advantages over other potentials, it does

not reproduce the phase diagram with quantitative accuracy. Due to this limitation, the Al-Si simulations reported in this paper are not expected to make quantitatively accurate predictions for this system. Rather, our goal is to explore general interface diffusion trends in a model metal-nonmetal system featuring a simple eutectic phase diagram.

3.2 Interphase boundary structures

Over a dozen crystallographically distinct Al-Si interphase boundaries were studied in this work. They were created by either the direct bonding method or by simulated epitaxy and equilibrated as described in section 2.2.

A first key finding is that many interfaces with general crystallography recrystallize into more stable crystallographic orientation relationships at high temperatures in a process that we call interface-induced recrystallization. An example is shown in Fig. 1 for the $\{851\}_{\text{Al}} \parallel \{310\}_{\text{Si}}$ interface. Upon annealing the initial interface for several ns, a new Al grain nucleates at the interface with a cube orientation relationship $\{310\}_{\text{Al}} \parallel \{310\}_{\text{Si}}$. Growth of the new grain occurs by rapid migration of a newly formed Si-enriched GB into the parent Al grain. Si concentration at the new GB is around 26 at.%, which is close to the eutectic liquid composition (27 at.%Si). The interphase boundary left behind the moving GB is strongly faceted and atomically sharp. Other general interphase boundaries were also observed to recrystallize into thin, faceted structures with near-cube orientation relationships (see Table 1). Interesting additional features of the interface-induced recrystallization phenomenon, such as solute drag during the GB migration and the misfit strain dependence of this process, are discussed in the Supplementary Information file.

A second key finding is that only a small set of interfaces with high-symmetry orientation relationships were stable at high temperatures. We obtained a set of stable interfaces via multiple processing methods, including direct bonding, recrystallization, and simulated epitaxy. Table 1 summarizes all stable interfaces found in this work. The stable orientation relationships produced by epitaxy simulations are graphically summarized in Fig. 2 for a range of Si substrate orientations. The stable orientation relationships are either cube-type or twin-related and are in good agreement with epitaxy experiments [56]. For example, both the $\{111\}_{\text{Al}} \parallel \{111\}_{\text{Si}}$ and $\{110\}_{\text{Al}} \parallel \{001\}_{\text{Si}}$ interfaces remained stable in our simulations at high temperatures and have also been found predominant over a range of temperatures in epitaxy experiments [56–58]. Recent simulation studies of near-eutectic Al-Si alloys also suggest a predominance of cube orientation relationships [38], which is consistent with our results.

An intriguing feature of the interfaces produced by recrystallization and epitaxy is the lattice rotations away from the exact cube or twin-related orientations. The magnitudes of such rotations vary from 0 to 11 degrees and disagree across the processing methods.

For example, epitaxially deposited interfaces exhibit larger rotations away from the cube orientation and have less pronounced faceted structures than recrystallized interfaces. The rotations away from the exact cube or twin-related orientations are reminiscent of the lattice rotations observed in epitaxy studies of FCC-FCC metallic systems [59–61]. The structures constructed by direct bonding are constrained to have zero disorientation. They also tend to have less pronounced faceting than recrystallized structures. These observations demonstrate a rich multiplicity of possible metastable variants of the cube and twin-related interphase boundaries.

Deviations from perfect interface equilibrium were also revealed in the form of additional defects in some of the interfaces, such as disconnections and threading dislocations (Fig. 3). These additional defects remained stable on the MD timescales accessible to us (up to 100 ns) and served as additional “short-circuit” pathways for diffusion. An example of interface disconnections is shown in Fig. 3a for the $\{110\}_{\text{Al}} \parallel \{001\}_{\text{Si}}$ interface constructed by the direct bonding method. Crystallographic characterization of the disconnections is given in the Supplementary Information file (Supplementary Fig. 3). The same interface produced by simulated epitaxy exhibits threading dislocations with perfect screw $1/2 \langle 110 \rangle$ character, which dissociate into Shockley partials near the interface. These examples demonstrate various ways by which the Burgers vector content of an interphase boundary can be redistributed and localized.

Melting behavior of the interfaces was examined at a range of temperatures just below and above the eutectic temperature. It was found that, in all cases, superheating was required (often by 100 K or more) to cause melting on the MD timescales. Melting was observed to nucleate at interface defects such as disconnections or facet junctions. In previous work, two classes of interfaces were distinguished based on whether pre-melting was observed before the bulk melting temperature (disordered interfaces) or upon superheating (ordered interfaces) [62]. The absence of pre-melting indicates that the Al-Si interphase boundaries studied in this work are well-ordered interfaces similar to coherent GBs.

3.3 Diffusion coefficients and mechanisms

Diffusion in stable Al-Si interfaces was found to be very slow on the MD timescale. Although some atomic hops were observed in the interface region during long anneals, this atomic motion was insufficient for reaching the diffusive regime in which the Einstein relation would hold. Facet junctions at nano-faceted interfaces did not exhibit sufficient atomic mobility either. The lower limit of diffusion coefficients that could be measured in this work is about $D = 10^{-13} \text{ m}^2/\text{s}$. This number provides an upper estimate of possible Al-Si interface diffusion coefficients.

The diffusive regime was successfully reached only for the $\{110\}_{\text{Al}} \parallel \{001\}_{\text{Si}}$ interface

containing a disconnection dipole. The interface diffusion coefficients were extracted from the slopes of MSD versus time curves illustrated in Fig. 4a. The curves display some degree of diffusion intermittency manifested by the slight wiggles. However, this intermittency is much weaker than the one observed for Al GB diffusion [63], which was caused by point-defect avalanches in the GB core. Collective diffusion mechanisms in the disconnection core were visually apparent from atomic displacement fields revealing string-like displacements of both Al and Si atoms parallel to the disconnection lines (Fig. 4c). Disconnection diffusion occasionally produced displacement cascades in nearby lattice regions, which took winding paths through the Al grain before returning into the disconnection (Fig. 4b). Similar excursions of point defects into the lattice were previously observed in MD simulations of dislocation diffusion in Al [64]. In this work, such excursions were also found during Al GB diffusion, although they were not as frequent as for disconnection diffusion.

Disconnection diffusion mechanisms exhibit the familiar hallmarks of dynamical heterogeneity, including spontaneous formation and dissolution of string-like clusters of mobile atoms (Fig. 5a-c). Examples of string-like displacement clusters are shown in Fig. 5b-c for the time interval t^* at which the average string length attains a maximum (Fig. 5a). The string-like clusters have a fractal dimension of 1.5, which is halfway between a linear chain and a random walk in 2D. A similar fractal dimension was found in previous simulations of GB diffusion in FCC Cu [65]. Individual atomic displacements tend to have components along $\langle 110 \rangle$ directions, as shown in the displacement orientation probability distribution in Fig. 5e. Although Al atoms are the dominant participants in the string-like motion, Si atoms are also involved in the strings. For example, the linear chain of Al atomic displacements shown at the top of Fig. 5c stops at a Si atom, which only hops a short distance in the same direction. Si atoms also participate in ring-like diffusion mechanisms and other collective events. Pure Si strings of up to 4 atoms were observed, while some Al strings comprised over 40 atoms (Fig. 5f). This contrast in the degree of participation suggests that Si diffusion is associated with a smaller length scale of collective motion compared with Al diffusion. We hypothesize that Si atoms interrupt the collective mechanisms that would otherwise have an even larger scale in Al GB disconnections.

Diffusion coefficients in the Al-Si interphase boundaries and several reference systems are shown on the Arrhenius diagram (log diffusivity versus inverse temperature) in Fig. 6. The reference systems include pure Al and pure Si GBs, pure Al and pure Si liquids, the eutectic liquid, and a Si-enriched Al GB. We also include experimental data for indirect measurements of Si dislocation diffusion in Al [66]. Experimental data and DFT calculations are also shown for lattice diffusion in pure Al and Si diffusion in Al-Si alloys. Table 2 summarizes the diffusion activation energies and prefactors for each system. For the Al-Si interface with disconnections, the phase compositions vary with temperature along the solvus lines on the phase diagram. Thus, the temperature dependence of the Al and

Si diffusivities is not expected to follow the Arrhenius law. Given also that the calculations include only three temperatures in a narrow temperature interval, we refrained from predicting the Arrhenius parameters in this case.

The main conclusion from Fig. 6 is that the Al-Si interphase boundaries suppress Al diffusion relative to Al GBs and accelerate Si diffusion relative to Si GBs. The comparison with GBs requires an explanation because GB diffusivities span several orders of magnitude, depending on the GB type. Out of the six Al GBs studied in this work, the $\Sigma 3$ (211) incoherent twin boundary and the (100)|| (110) incommensurate GB have the lowest diffusion coefficients, the highest activation energies, and do not exhibit any significant pre-melting. They represent the lower envelope of diffusion coefficients in high-angle GBs in Al and can be used for comparison with interphase boundaries. The incommensurate GB has the same macroscopic crystallography as the $\{110\}_{\text{Al}} || \{001\}_{\text{Si}}$ interphase boundary. The interphase boundary produced by simulated epitaxy is atomically flat and has such a low diffusivity that it could not be resolved by MD simulations. It certainly lies below the diffusivity of even the slowest-diffusion GBs in Al. The direct bonding method produces a metastable structure of this interface that contains disconnections, which increase the rates of both Al and Si diffusion. This disconnection-accelerated interface diffusivity is comparable with the Al diffusivity in the incommensurate and incoherent twin GBs. In other words, it reaches the lower bound of Al GB diffusivities.

The results shown in Fig. 6 indicate that Si diffusivity tends to increase in the order: Si crystal \rightarrow Si GBs \rightarrow Si in Al lattice \rightarrow Si in planar Al-Si interface \rightarrow Si in Al-Si interface with disconnections \rightarrow Si in Al GBs \rightarrow Si in Si-Al liquid. In particular, the extrapolated rate of Si diffusion in the Si $\Sigma 17$ $\langle 100 \rangle$ GB falls well below Si diffusivity in the Al-Si interface with disconnections and likely below the Si diffusivity in the interface without disconnections. To evaluate the Si diffusivity in Al GBs, we used a Si-enriched Al GB obtained by interface-induced recrystallization when the new GB remained immobile after splitting from the Al-Si interface. The Al and Si diffusion coefficients in this GB fall in the upper range of GB diffusion coefficients in high-angle Al GBs. A more systematic test was performed by studying diffusion in the $\Sigma 17$ and $\Sigma 3$ GBs in Al-8at.%Si alloy (Fig. 7a). Si atoms were observed to strongly segregate to these GBs and form a 1 nm or thicker disordered (liquid-like) layer with eutectic composition (Fig. 8a, bottom panel). The liquid-like nature of the segregated layer was confirmed by the shift of the radial distribution function toward the one for the eutectic liquid (Fig. 8a). Both Al and Si were found to diffuse significantly faster in the segregated GBs than Al self-diffusion in pure Al GBs with the same crystallography (Fig. 7a). Si is observed to diffuse in the segregated GBs slightly faster than Al (7b), mirroring a similar trend in crystalline Al and eutectic liquid. In all these cases, the Si diffusivity far exceeds its diffusivity in Al-Si interfaces.

Finally, we note that diffusion coefficients in the eutectic liquid show a downward devia-

tion from the Arrhenius law (Fig. 6) reminiscent of that in fragile glass-forming liquids [52]. As in the studies of model fragile metallic glasses [67], percolating networks of icosahedrally coordinated atoms were apparent in the structure of the deeply supercooled Al-Si liquid. Crystallization of the eutectic liquid was observed at sufficiently low temperatures (around $0.6 T_{\text{eu}}$).

4 Discussion

Over the past two decades, new atomistic methods have been developed to accurately calculate GB diffusion coefficients and better understand atomic-level GB diffusion mechanisms [51, 63, 65, 68–75]. To our knowledge, this work is the first application of such methods to diffusion along metal-nonmetal interphase boundaries.

The main discovery of this work is that the diffusion mobilities of Al and Si atoms in stable Al-Si interphase boundaries are much lower than their mobilities in Al GBs (Fig. 6). They are also lower than the mobilities in interphase boundary disconnections existing in metastable interface structures. In fact, the diffusivity in stable planar interphase boundaries is so low that we could not quantify it by MD simulations. We could only estimate an upper bound of possible interface diffusion coefficients (Fig. 6).

We hypothesize that the sluggish interphase boundary diffusion is a common feature of interfaces between highly dissimilar materials with significantly different chemical bond strengths. In our case, Si is a covalently bonded material with a significantly higher melting temperature and greater mechanical strength than metallic Al. Al-Si interfaces can only exist below the eutectic temperature $T_{\text{eu}} = 850$ K [53], which corresponds to the homologous temperature of 0.91 for Al and 0.50 for Si. In other words, the eutectic temperature is very hot for Al and very cold for Si. Accordingly, at temperatures close to T_{eu} , the mobility of Al atoms is very high in both Al GBs and FCC lattice, while the Si mobility is drastically lower in both Si GBs and DC lattice. Although the interatomic potential used in this work underestimates the experimental eutectic temperature, it correctly reproduces this basic feature of the Al-Si system, including the large mobility gap between Al and Si.

The Si atoms residing on the Si side of the Al-Si interfaces are virtually immobile on the diffusion timescale of Al atoms. The strongly ordered Si positions impose a periodic potential that restrains the motion of both Al and Si atoms along the interface, suppressing the interface diffusivity. By contrast, both Al and Si atoms diffusing along Al GBs are free from the mentioned constraint, leading to higher mobility relative to the interphase boundaries (Figs. 6 and 7). For the same reason, at temperatures on the order of T_{eu} , Si diffusivity in FCC Al is much higher than in the DC Si lattice, where the atoms are subject to the strong ordering constraint. This explanation of the sluggishness of the Al-Si interface diffusion is purely qualitative and requires a more rigorous quantitative formulation in the

future.

Even when the interface diffusivity was too low to calculate the diffusion coefficients, diffusion mechanisms could still be observed. We find that the interface atoms diffuse predominantly by collective rearrangements, often in the form of strings or rings of correlated displacements. Similar mechanisms were previously observed in the simulations of GB self-diffusion in elemental metals [63, 65, 68–71, 75]. In this work, we observed the operation of the collective mechanisms during the co-diffusion of two atomic species, Al and Si. Both species participate in the collective rearrangements, but to a different extent due to the difference in their mobilities. Si atoms participate in collective events to a lesser extent than Al atoms. It also appears that they tend to disrupt the chains of Al displacements relative to those in pure Al environments.

One of the challenges in modeling interphase boundaries is constructing a two-phase system in full thermodynamic equilibrium and finding the orientation relationships corresponding to the most stable interface structures. This task requires close integration of MD and MC methodologies and constituted a significant part of the present work. One of the unexpected findings was the phenomenon of interface-induced recrystallization. An interface brought to a non-equilibrium state by thermal processing or deformation can transform to a more stable state by changing the orientation relationship between the phases and injecting a new grain into the metallic phase. This process and its possible impact on the mechanical properties of metal-ceramic composites is worth further exploration by experiment and modeling in the future.

5 Conclusions

We have studied the atomic structure, structural stability, and diffusion processes in Al-Si interphase boundaries by combining MD and MC simulations with an interatomic potential [42]. Two different interface preparation methods were applied: direct bonding and simulated epitaxy. Diffusion coefficients in the interphase boundaries were calculated and compared with those in Al GBs and bulk liquid. Interface diffusion mechanisms were investigated by statistical methods developed previously for GBs and supercooled glass-forming liquids. The following conclusions can be drawn from this work.

(1) The most stable interphase boundaries were found to be either planar or nano-faceted and tended to have either cubic or twin-related orientation relationships. Many of the orientation relationships found in this work were previously observed in experiments. The stable interfaces did not pre-melt and could be overheated above the eutectic temperature.

(2) Diverse metastable interface structures were observed, depending on the fabrication method and lattice misfit. Examples include interfaces with disconnections and interfaces shooting out threading dislocations into the metallic phase. Disconnections were found to

accelerate interface diffusion, while the facet edges did not. The impact of other interface defects, such as absorbed lattice dislocations, on interface diffusion and other properties of Al-Si composites is yet to be studied.

(3) The simulations have revealed an interesting phenomenon of interface-induced recrystallization of the metallic phase. The new metallic grains can be nanometer-scale thin or can grow deep into the metallic phase. The moving GBs bounding the growing grain carry along some of the Si atoms and can be slowed down by the solute drag effect. We envision that interface-induced recrystallization may occur in metal-matrix composites during high-temperature creep deformation. The effect resembles the diffusion-induced recrystallization previously observed in diverse systems [76–78].

(4) Diffusion of Al and Si atoms in stable Al-Si interfaces is surprisingly slow and could not be calculated on the MD timescale accessible to us. We estimate that the interface diffusivities are below $D = 10^{-13}$ m²/s even at the eutectic temperature. The interphase boundary diffusion is much slower than diffusion of both Al and Si in Al GBs. On the other hand, disconnections existing in metastable interface structures greatly accelerate diffusion to a level where it can be readily calculated and was found to be close to the diffusivity in some of the Al GBs. We suggest that this observation could be relevant to the loss of creep resistance of composites at high temperatures. If the initial interface sliding creates a set of interface dislocations and/or disconnections, the accelerated interface diffusion will promote further sliding, triggering a self-amplified process that eventually causes the loss of sliding resistance.

(5) The sluggish interphase boundary diffusion could be a common feature of many metal-ceramic systems with significantly different bond strengths, melting temperatures, and thus diffusivities in the two phases. The highly ordered atomic structure of the ceramic phase can suppress the diffusion mobility in the interface region relative to the less constrained atomic environments in metallic GBs. This can qualitatively explain the faster GB diffusion than diffusion along the interphase boundaries. In the Al-Si system, the additional effect is the disordering of Al GBs caused by Si segregation, resulting in further acceleration of GB diffusion.

(6) Similar to GB diffusion, diffusion in interphase boundaries is dominated by correlated atomic rearrangements involving strings and rings of simultaneously moving atoms. Both Al and Si atoms participate in the collective mechanisms, although to a different extents. Collective mechanisms of interface co-diffusion of two or more species with different mobilities is an interesting topic for future research.

(7) The interatomic potential [42] used in this work reproduces the Al-Si phase diagram qualitatively correctly but underestimates the eutectic temperature and overestimates the solubility limits in the solid Al and Si. A more accurate interatomic potential for this system should be developed to ensure quantitatively accurate simulation results.

Acknowledgements

This research was supported by the U.S. Department of Energy, Office of Basic Energy Sciences, Division of Materials Sciences and Engineering, under Award # DE-SC0023102.

References

- [1] A. P. Sutton and R. W. Balluffi. *Interfaces in Crystalline Materials*. Clarendon Press, Oxford, 1995.
- [2] J. M. Howe. *Interfaces in Materials*. John Wiley & Sons, NY, 1997.
- [3] Yuntian Zhu, Kei Ameyama, Peter M. Anderson, Irene J. Beyerlein, Huajian Gao, Hyoungh Seop Kim, Enrique Lavernia, Suveen Mathaudhu, Hael Mughrabi, Robert O. Ritchie, Nobuhiro Tsuji, Xiangyi Zhang, and Xiaolei Wu. Heterostructured materials: superior properties from hetero-zone interaction. *Materials Research Letters*, 9(1):1–31, 01 2021.
- [4] W. Wunderlich. The atomistic structure of metal/ceramic interfaces is the key issue for developing better properties. *Metals*, 4:410–427, 2014.
- [5] Zaoli Zhang, Yao Long, S. Cazottes, R. Daniel, C. Mitterer, and G. Dehm. The peculiarity of the metal-ceramic interface. *Scientific Reports*, 5(1):11460, 2015.
- [6] Mohsen Damadam, Shuai Shao, Iman Salehinia, Georges Ayoub, and Hussein M. Zbib. Molecular dynamics simulations of mechanical behavior in nanoscale ceramic–metallic multilayer composites. *Materials Research Letters*, 5(5):306–313, 09 2017.
- [7] L. W. Yang, C. Mayer, N. Li, J. K. Baldwin, N. A. Mara, N. Chawla, J. M. Molina-Aldareguia, and J. Llorca. Mechanical properties of metal-ceramic nanolaminates: Effect of constraint and temperature. *Acta Materialia*, 142:37–48, 2018.
- [8] Markus J. Buehler and Amit Misra. Mechanical behavior of nanocomposites. *MRS Bulletin*, 44(1):19–24, 2019.
- [9] Binbin Xu, Wenxiang Xu, and Fenglin Guo. Creep behavior due to interface diffusion in unidirectional fiber-reinforced metal matrix composites under general loading conditions: a micromechanics analysis. *Acta Mechanica*, 231(4):1321–1335, 2020.
- [10] Huai-Hsun Lien, Jyoti Mazumder, Jian Wang, and Amit Misra. Ultrahigh strength and plasticity in laser rapid solidified Al–Si nanoscale eutectics. *Materials Research Letters*, 8(8):291–298, 08 2020.

- [11] Jaafar Abboud and Jyoti Mazumder. Developing of nano sized fibrous eutectic silicon in hypereutectic Al–Si alloy by laser remelting. *Scientific Reports*, 10(1):12090, 2020.
- [12] Huai-Hsun Lien, Jian Wang, and Amit Misra. Plastic deformation induced microstructure transition in nano-fibrous Al-Si eutectics. *Materials & Design*, 218:110701, 2022.
- [13] Y. L. Shen and S. Suresh. Steady-state creep of metal-ceramic multilayered materials. *Acta Mater.*, 44:1337–1348, 1996.
- [14] S. Ranganath and R. S. Mishra. Steady state creep behavior of particle-reinforced titanium matrix composites. *Acta Mater.*, 44:927–935, 1996.
- [15] Farghalli A. Mohamed and Yong Li. Creep and superplasticity in nanocrystalline materials: current understanding and future prospects. *Mater. Sci. Eng. A*, 298:1–15, 2001.
- [16] Yi Huang and Terence Langdon. The creep behavior of discontinuously reinforced metal-matrix composites. *JOM*, 55:15–20, 05 2003.
- [17] J. Rösler, G. Bao, and A. G. Evans. The effects of diffusional relaxation on the creep strength of composites. *Acta Metallurgica et Materialia*, 39(11):2733–2738, 1991.
- [18] J. V. Funn and I. Dutta. Creep behavior of interfaces in fiber reinforced metal–matrix composites. *Acta Materialia*, 47(1):149–164, 1998.
- [19] I Dutta. Role of interfacial and matrix creep during thermal cycling of continuous fiber reinforced metal–matrix composites. *Acta Materialia*, 48(5):1055–1074, 2000.
- [20] K. A. Peterson, I. Dutta, and M. W. Chen. Diffusionally accommodated interfacial sliding in metal-silicon systems. *Acta Materialia*, 51(10):2831–2846, 2003.
- [21] K. A. Peterson, I. Dutta, and M. W. Chen. Measurement of creep kinetics at Al-Si interfaces. *Scripta Materialia*, 47(10):649–654, 2002.
- [22] K. A Peterson, I Dutta, and M Chen. Processing and characterization of diffusion-bonded Al-Si interfaces. *Journal of Materials Processing Technology*, 145(1):99–108, 2004.
- [23] M. W. Chen and I. Dutta. Atomic force microscopy study of plastic deformation and interfacial sliding in Al thin film: Si substrate systems due to thermal cycling. *Applied Physics Letters*, 77(26):4298–4300, 2020/10/07 2000.

- [24] I. Dutta, M. W. Chen, K. Peterson, and T. Shultz. Plastic deformation and interfacial sliding in Al and Cu thin film: Si substrate systems due to thermal cycling. *Journal of Electronic Materials*, 30(12):1537–1548, 2001.
- [25] I. Kaur, W. Gust, and L. Kozma. *Handbook of Grain and Interphase Boundary Diffusion Data*. Ziegler, Stuttgart, 1989.
- [26] I. Kaur, Y. Mishin, and W. Gust. *Fundamentals of Grain and Interphase Boundary Diffusion*. Wiley, Chichester, West Sussex, 1995.
- [27] J. Sommer, T. Muschik, Chr. Herzig, and W. Gust. Silver tracer diffusion in oriented AgCu interphase boundaries and correlation to the boundary structure. *Acta Materialia*, 44(1):327–334, 1996.
- [28] Chr. Minkwitz, Christian Herzig, Boris B. Straumal, and W. Gust. Radiotracer diffusion of Ni and Ag in Ag and Ni grain boundaries and oriented Ag/Ni interphase boundaries. *Materials Science Forum*, 294-296:541–544, 1998.
- [29] B. B. Straumal, L. M. Klinger, and L. S. Shvindlerman. The effect of crystallographic parameters of interphase boundaries on their surface tension and parameters of the boundary diffusion. *Acta Metallurgica*, 32(9):1355–1364, 1984.
- [30] Anna Kosinova, Oleg Kovalenko, Leonid Klinger, and Eugen Rabkin. Mechanisms of solid-state dewetting of thin Au films in different annealing atmospheres. *Acta Materialia*, 83:91–101, 2015.
- [31] Aakash Kumar, Hagit Barda, Leonid Klinger, Michael W Finnis, Vincenzo Lordi, Eugen Rabkin, and David J Srolovitz. Anomalous diffusion along metal/ceramic interfaces. *Nature communications*, 9(1):1–8, 2018.
- [32] Hagit Barda and Eugen Rabkin. Metal hetero-diffusion along the metal-ceramic interfaces: A case study of Au diffusion along the Ni-sapphire interface. *Acta Materialia*, 186:242–249, 2020.
- [33] H. Mehrer. *Diffusion in Solids: Fundamentals, Methods, Materials*. Springer Verlag, Berlin, 2007.
- [34] I. Salehinia, S. Shao, J. Wang, and H. M. Zbib. Plastic deformation of metal/ceramic nanolayered composites. *JOM*, 66(10):2078–2085, 2014.
- [35] Mohsen Damadam, Shuai Shao, Iman Salehinia, Ioannis Mastorakos, Georges Ayoub, and Hussein M. Zbib. Strength and plastic deformation behavior of nanolaminate

- composites with pre-existing dislocations. *Computational Materials Science*, 138:42–48, 2017.
- [36] Adnan Rasheed and Iman Salehinia. Atomistic simulation of scratch behavior of ceramic/metal (cermet) nanolaminates. In *MRS Advances*, volume 2, pages 3571–3576. Materials Research Society, 2017.
- [37] Jian Wang, Qing Zhou, Shuai Shao, and Amit Misra. Strength and plasticity of nanolaminated materials. *Materials Research Letters*, 5(1):1–19, 01 2017.
- [38] Wenqian Wu, Mingyu Gong, Bingqiang Wei, Amit Misra, and Jian Wang. Atomistic modeling of interface strengthening in Al-Si eutectic alloys. *Acta Materialia*, 225:117586, 2022.
- [39] Amit Misra, Mathias Göken, Nathan A. Mara, and Irene J. Beyerlein. Hierarchical and heterogeneous multiphase metallic nanomaterials and laminates. *MRS Bulletin*, 46(3):236–243, 2021.
- [40] A. P. Thompson, H. M. Aktulga, R. Berger, D. S. Bolintineanu, W. M. Brown, P. S. Crozier, P. J. in 't Veld, A. Kohlmeyer, S. G. Moore, T. D. Nguyen, R. Shan, M. J. Stevens, J. Tranchida, C. Trott, and S. J. Plimpton. LAMMPS - a flexible simulation tool for particle-based materials modeling at the atomic, meso, and continuum scales. *Comp. Phys. Comm.*, 271:108171, 2022.
- [41] Alexander Stukowski. Visualization and analysis of atomistic simulation data with OVITO – the open visualization tool. *Modelling and simulation in materials science and engineering*, 18(1):015012, 2009.
- [42] P Saidi, T Frolov, JJ Hoyt, and M Asta. An angular embedded atom method interatomic potential for the aluminum–silicon system. *Modelling and Simulation in Materials Science and Engineering*, 22(5):055010, 2014.
- [43] Axel Kohlmeyer. lammeps plug-ins package, 2022.
- [44] Yuri Mishin. Atomistic modeling of the gamma and gamma-prime phases of the Ni–Al system. *Acta Materialia*, 52(6):1451–1467, 2004.
- [45] GP Purja Pun and Y Mishin. Development of an interatomic potential for the Ni-Al system. *Philosophical Magazine*, 89(34-36):3245–3267, 2009.
- [46] PL Williams, Y Mishin, and JC Hamilton. An embedded-atom potential for the Cu–Ag system. *Modelling and Simulation in Materials Science and Engineering*, 14(5):817, 2006.

- [47] CA Howells and Y Mishin. Angular-dependent interatomic potential for the binary Ni–Cr system. *Modelling and Simulation in Materials Science and Engineering*, 26(8):085008, 2018.
- [48] Peter Mahler Larsen, Søren Schmidt, and Jakob Schiøtz. Robust structural identification via polyhedral template matching. *Modelling and Simulation in Materials Science and Engineering*, 24(5):055007, 2016.
- [49] James Hickman and Yuri Mishin. Thermal conductivity and its relation to atomic structure for symmetrical tilt grain boundaries in silicon. *Physical Review Materials*, 4(3):033405, 2020.
- [50] CP Race. Quantifying uncertainty in molecular dynamics simulations of grain boundary migration. *Molecular Simulation*, 41(13):1069–1073, 2015.
- [51] Hao Zhang, David J Srolovitz, Jack F Douglas, and James A Warren. Grain boundaries exhibit the dynamics of glass-forming liquids. *Proceedings of the National Academy of Sciences*, 106(19):7735–7740, 2009.
- [52] Hao Zhang, Xinyi Wang, Hai-Bin Yu, and Jack F Douglas. Dynamic heterogeneity, cooperative motion, and Johari–Goldstein β relaxation in a metallic glass-forming material exhibiting a fragile-to-strong transition. *The European Physical Journal E*, 44(4):1–30, 2021.
- [53] George F Vander Voort and Juan Asensio-Lozano. The Al-Si phase diagram. *Microscopy and Microanalysis*, 15(S2):60–61, 2009.
- [54] Avinash M Dongare, Bruce LaMattina, Douglas L Irving, Arunachalam M Rajendran, Mohammed A Zikry, and Donald W Brenner. An angular-dependent embedded atom method (A-EAM) interatomic potential to model thermodynamic and mechanical behavior of Al/Si composite materials. *Modelling and Simulation in Materials Science and Engineering*, 20(3):035007, 2012.
- [55] S Starikov, I Gordeev, Y Lysogorskiy, L Kolotova, and S Makarov. Optimized interatomic potential for study of structure and phase transitions in Si-Au and Si-Al systems. *Computational Materials Science*, 184:109891, 2020.
- [56] KH Westmacott, S Hinderberger, and U Dahmen. Physical vapour deposition growth and transmission electron microscopy characterization of epitaxial thin metal films on single-crystal Si and Ge substrates. *Philosophical Magazine A*, 81(6):1547–1578, 2001.
- [57] N Thangaraj, KH Westmacott, and U Dahmen. Epitaxial growth of (011) Al on (100) Si by vapor deposition. *Applied Physics Letters*, 61(1):37–39, 1992.

- [58] Brian M McSkimming, Ashish Alexander, Margaret H Samuels, Bruce Arey, Ilke Arslan, and Christopher JK Richardson. Metamorphic growth of relaxed single crystalline aluminum on silicon (111). *Journal of Vacuum Science & Technology A: Vacuum, Surfaces, and Films*, 35(2):021401, 2017.
- [59] Paul Wynblatt and Dominique Chatain. Importance of interfacial step alignment in hetero-epitaxy and orientation relationships: the case of Ag equilibrated on Ni substrates. Part 1 computer simulations. *Journal of Materials Science*, 50(15):5262–5275, 2015.
- [60] Dominique Chatain, Paul Wynblatt, Anthony D Rollett, and Gregory S Rohrer. Importance of interfacial step alignment in hetero-epitaxy and orientation relationships: the case of Ag equilibrated on Ni substrates. Part 2 experiments. *Journal of Materials Science*, 50(15):5276–5285, 2015.
- [61] Paul Wynblatt, Dominique Chatain, and Ulrich Dahmen. Heteroepitaxy of fcc-on-fcc systems of large misfit. *Acta Materialia*, 225:117550, 2022.
- [62] Ming Tang, W Craig Carter, and Rowland M Cannon. Diffuse interface model for structural transitions of grain boundaries. *Physical Review B*, 73(2):024102, 2006.
- [63] Ian Chesser and Yuri Mishin. Point-defect avalanches mediate grain boundary diffusion. *Communications Materials*, 3(1):90, 2022.
- [64] G. P. Purja Pun and Y. Mishin. A molecular dynamics study of self-diffusion in the cores of screw and edge dislocations in aluminum. *Acta Mater.*, 57:5531–5542, 2009.
- [65] Yuri Mishin. An atomistic view of grain boundary diffusion. In *Defect and Diffusion Forum*, volume 363, pages 1–11. Trans Tech Publ, 2015.
- [66] Marc Legros, Gerhard Dehm, Eduard Arzt, and T John Balk. Observation of giant diffusivity along dislocation cores. *Science*, 319(5870):1646–1649, 2008.
- [67] PM Derlet, H Bocquet, and Robert Maaß. Viscosity and transport in a model fragile metallic glass. *Physical Review Materials*, 5(12):125601, 2021.
- [68] M. R. Sørensen, Y. Mishin, and A. F. Voter. Diffusion mechanisms in Cu grain boundaries. *Phys. Rev. B*, 62(6):3658–3673, 2000.
- [69] A. Suzuki and Y. Mishin. Atomistic modeling of point defects and diffusion in copper grain boundaries. *Interface Science*, 11:131–148, 2003.
- [70] A. Suzuki and Y. Mishin. Diffusion mechanisms in grain boundaries. *J. Metastable and Nonocryst. Mater.*, 19:1–24, 2004.

- [71] A. Suzuki and Y. Mishin. Atomic mechanisms of grain boundary diffusion: Low versus high temperatures. *J. Mater. Sci.*, 40:3155–3161, 2005.
- [72] T. Frolov, S. V. Divinski, M. Asta, and Y. Mishin. Effect of interface phase transformations on diffusion and segregation in high-angle grain boundaries. *Phys. Rev. Lett.*, 110:255502, 2013.
- [73] R. K. Koju and Y. Mishin. Relationship between grain boundary segregation and grain boundary diffusion in Cu-Ag alloys. *Phys. Rev. Materials*, 4:073403, 2020.
- [74] R. K. Koju and Y. Mishin. Atomistic study of grain-boundary segregation and grain-boundary diffusion in Al-Mg alloys. *Acta Materialia*, 201:596–603, 2020.
- [75] S Starikov, M Mrovec, and R Drautz. Study of grain boundary self-diffusion in iron with different atomistic models. *Acta Materialia*, 188:560–569, 2020.
- [76] Ki-Woong Chae, Cheol Seong Hwang, Doh-Yeon Kim, and Seong-Jai Cho. Diffusion induced recrystallization of TiC. *Acta materialia*, 44(5):1793–1799, 1996.
- [77] G Schmitz, D Baither, M Kasprzak, TH Kim, and B Kruse. The hidden link between diffusion-induced recrystallization and ideal strength of metals. *Scripta Materialia*, 63(5):484–487, 2010.
- [78] Mor Levi, Anuj Bisht, and Eugen Rabkin. Diffusion-induced recrystallization during the early stages of solid-state dewetting of Ni-Pt bilayers. *Acta Materialia*, 225:117537, 2022.
- [79] Wei Zhong, Mohammad Shahriar Hooshmand, Maryam Ghazisaeidi, Wolfgang Windl, and Ji-Cheng Zhao. An integrated experimental and computational study of diffusion and atomic mobility of the aluminum–magnesium system. *Acta Materialia*, 189:214–231, 2020.
- [80] MS Hooshmand, W Zhong, JC Zhao, W Windl, and M Ghazisaeidi. Data on the comprehensive first-principles diffusion study of the aluminum-magnesium system. *Data in Brief*, 30:105381, 2020.
- [81] Shin-Ichiro Fujikawa, Ken-Ichi Hirano, and Yoshiaki Fukushima. Diffusion of silicon in aluminum. *Metallurgical Transactions A*, 9(12):1811–1815, 1978.
- [82] Yong Du, Y. A Chang, Baiyun Huang, Weiping Gong, Zhanpeng Jin, Honghui Xu, Zhaohui Yuan, Yong Liu, Yuehui He, and F. Y Xie. Diffusion coefficients of some solutes in fcc and liquid Al: critical evaluation and correlation. *Materials Science and Engineering: A*, 363(1):140–151, 2003.

- [83] Tobias Südkamp and Hartmut Bracht. Self-diffusion in crystalline silicon: A single diffusion activation enthalpy down to 755° C. *Physical Review B*, 94:125208, 2016.
- [84] Florian Strauß, Lars Dörrer, Thomas Geue, Jochen Stahn, Alexandros Koutsioubas, Stefan Mattauch, and Harald Schmidt. Self-diffusion in amorphous silicon. *Physical review letters*, 116(2):025901, 2016.
- [85] MI Mendeleev, MJ Kramer, Chandler A Becker, and M Asta. Analysis of semi-empirical interatomic potentials appropriate for simulation of crystalline and liquid Al and Cu. *Philosophical Magazine*, 88(12):1723–1750, 2008.
- [86] R.K. Koju and Y. Mishin. Direct atomistic modeling of solute drag by moving grain boundaries. *Acta Mater.*, 198:111–120, 2020.

Si (hkl)	Processing	Al-Si OR	Disorientation	Reconstructions
(1 1 1)	Epitaxy	Cube	$[-0.22, 0.77, 0.59]$ 0.1°	
	Direct bonding	Cube	0°	
(1 0 0)	Epitaxy	Twin-related	$[-0.68, -0.68, 0.28]$ 62.8°	Threading screw dislocations
	Direct bonding	Twin-related	$[-0.68, 0.28, 0.68]$ 62.8°	Disconnections
	Direct bonding	Cube	0°	Nano-facets
(1 1 0)	Epitaxy	Twin-related	$[1, 0, -1]$ 59.8°	
	Direct bonding	Cube	0°	
(1 1 2)	Epitaxy	Cube-related	$[-0.62, 0.71, -0.26]$ 6.2°	
	Recrystallization	Cube-related	$[0.63, 0.69, -0.37]$ 4.7°	
	Direct bonding	Cube	0°	Stacking faults extended from interface
(3 1 0)	Epitaxy	Cube-related	$[0.7, 0.61, -0.36]$ 11.3°	
	Recrystallization	Cube-related	$[310]$ 0.2°	Nano-facets
(2 1 0)	Epitaxy	Cube-related	$[-0.72, -0.46, -0.52]$ 11.3°	
	Recrystallization	Cube-related	$[0.34, 0.8, -0.49]$ 1.9°	Nano-facets
(8 5 1)	Epitaxy	Cube-related	$[0.96, -0.18, 0.21]$ 8.5°	
	Direct bonding	Cube	0°	
(1 2 3)	Epitaxy	Cube-related	$[0.63, 0.12, 0.77]$ 8.9°	
(1 1 5)	Epitaxy	Cube-related	$[1, 1, 0]$ 11.1°	
(3 3 2)	Epitaxy	Cube-related	$[-0.3, -0.27, -0.91]$ 2.8°	

Table 1: Stable Al-Si interfaces studied in this work. The table shows Miller indices (hkl) of the Si phase, disorientation (indices and angle) of the Al phase, and the type of crystallographic orientation relationship (OR) between the two.

System	Direction	E (eV)	D_0 (m ² /s)
Si in Al dislocation* [66]		1.12	7×10^{-4}
Al grain boundaries:			
Al(110) Al(100)	110 110	0.87 ± 0.06	$(1.4_{-2.1}^{+2.9}) \times 10^{-5}$
	100 110	1.10 ± 0.07	$(3.1_{-5.9}^{+8.0}) \times 10^{-4}$
$\Sigma 3$ $\langle 110 \rangle$ tilt 70.5°	tilt axis	1.31 ± 0.03	$(3.89_{-1.2}^{+2.1}) \times 10^{-3}$
	⊥ tilt axis	1.45 ± 0.03	$(1.17_{-2.7}^{+4.8}) \times 10^{-2}$
$\Sigma 17$ $\langle 100 \rangle$ tilt 61.9°	tilt axis	0.72 ± 0.01	$(5.53_{-0.6}^{+1.1}) \times 10^{-6}$
	⊥ tilt axis	0.81 ± 0.01	$(2.09_{-0.17}^{+0.33}) \times 10^{-5}$
$\Sigma 51$ $\langle 551 \rangle$ tilt 180°	average	0.55 ± 0.02	$(4.5_{-1.2}^{+2.2}) \times 10^{-7}$
$\Sigma 21$ $\langle 531 \rangle$ asymmetric tilt 80.4°	average	0.44 ± 0.01	$(5.4_{-0.8}^{+1.6}) \times 10^{-7}$
$\Sigma 45$ $\langle 851 \rangle$ tilt 180°	average	0.34 ± 0.01	$(9.7_{-0.9}^{+1.8}) \times 10^{-8}$
Si grain boundaries:			
$\Sigma 17$ $\langle 100 \rangle$ tilt 61.9°	average	1.59 ± 0.05	$(1.9_{-1.0}^{+1.7}) \times 10^{-5}$
Solids:			
Al in Al* [79]		1.32	1.8×10^{-5}
Al in Al** [80]		1.25–1.35	$(0.542–2.42) \times 10^{-5}$
Si in Al* [81, 82]		1.41	2×10^{-4}
Si in Si, vacancy mechanism* [83]		4.65	1.1×10^{-2}
Si in Si, interstitialcy mechanism* [83]		4.83	5.5×10^{-2}
Si in amorphous Si* [84]		4.4 ± 0.3	1.5×10^5
Liquids:			
Al in liquid Al		0.227 ± 0.001	$(9.69_{-0.12}^{+0.24}) \times 10^{-8}$
Al in eutectic liquid		0.231 ± 0.001	$(1.03_{-0.01}^{+0.03}) \times 10^{-7}$
Si in eutectic liquid		0.218 ± 0.007	$(1.0_{-0.09}^{+0.17}) \times 10^{-7}$
Si in Si liquid		0.429 ± 0.007	$(1.60_{-0.09}^{+0.16}) \times 10^{-7}$

Table 2: Activation energies (E) and prefactors (D_0) for diffusion in Al-Si systems calculated in this work. Shown for comparison is literature data for *experiment and **DFT calculations.

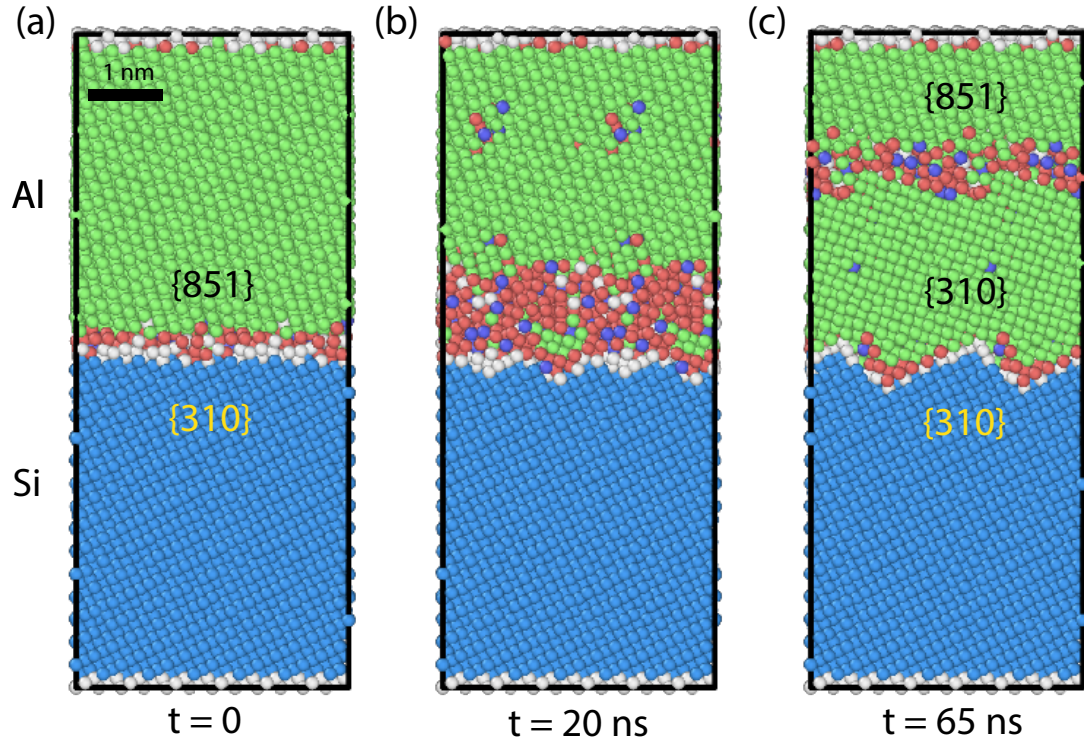


Figure 1: Example of interface-induced recrystallization in the Al-Si system at 650 K ($0.96T_{eu}$). MD time is indicated and atoms are colored by local coordination: green = FCC, blue = DC, and all other colors represent atoms in locally disordered environments. (a) Initial Al-Si interface at early stages of equilibration. (b) New Al grain nucleates at the interface. (c) Si-enriched GB migrates upward into Al, leaving a faceted Al-Si interface behind. The interface orientation relationships before and after recrystallization are indicated.

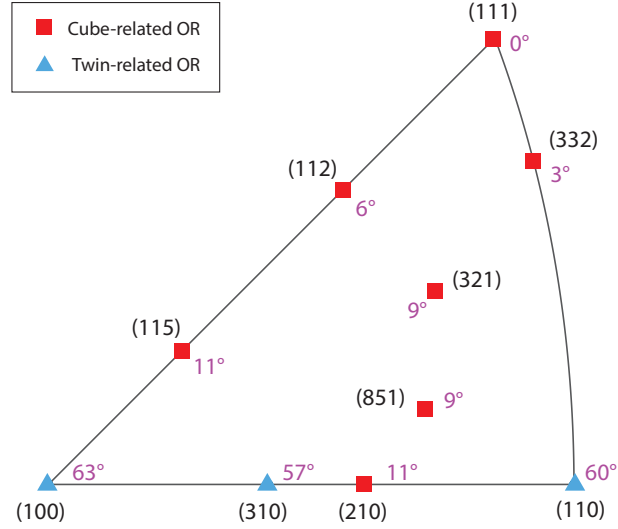


Figure 2: Crystallographic orientation relationships at Al-Si interfaces produced by simulated epitaxy. Si substrate orientations are indexed and plotted in the stereographic triangle. The disorientation angles (shown in purple) indicate deviations from the exact cube or twin orientations.

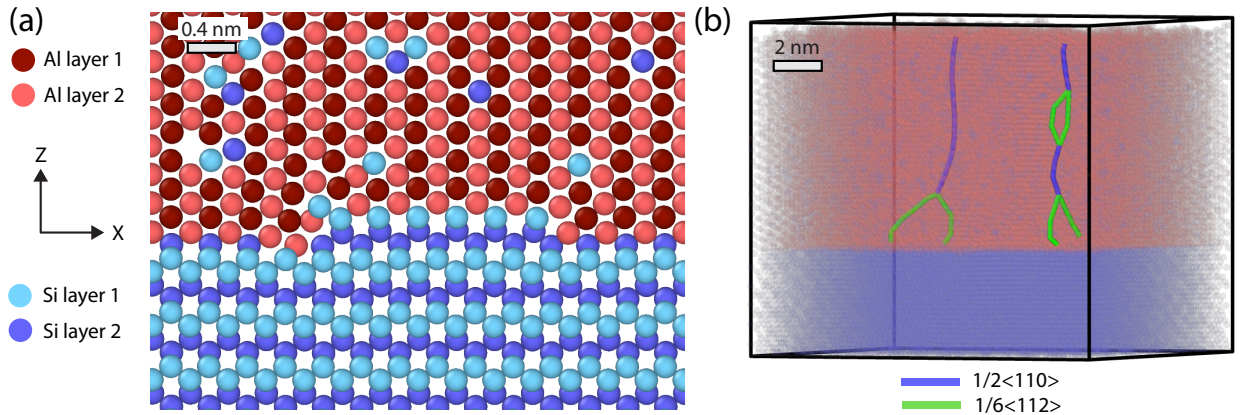


Figure 3: Examples of defects at Al-Si interfaces. The interface orientation is $\{110\}_{\text{Al}} \parallel \{001\}_{\text{Si}}$, with $\langle 100 \rangle_{\text{Al}} \parallel \langle 110 \rangle_{\text{Si}}$ along the X axis and $\langle 110 \rangle_{\text{Al}} \parallel \langle 110 \rangle_{\text{Si}}$ along the Y axis. The dark and light colors differentiate between atomic positions in alternating layers parallel to the page (X - Z plane). (a) Disconnection dipole in the directly bonded interface with 13:14 ratio of Al:Si periods in the X direction. The disconnection Burgers vector is 0.194 nm parallel to X (see Supplementary Fig. 3). (b) The same interface produced by simulated epitaxy with a larger (10 nm by 10 nm) cross-section does not contain disconnections but creates threading screw dislocations in the Al grain, which dissociate into partials at the interface. Both structures were observed at 650 K ($0.96 T_{\text{eu}}$).

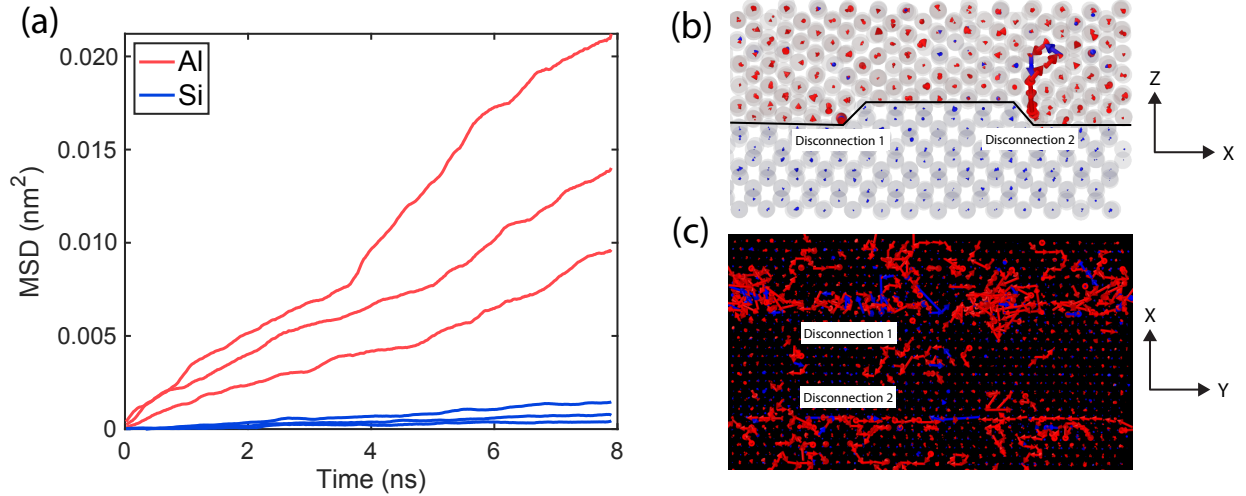


Figure 4: Calculation of diffusion coefficients in the Al-Si interphase boundary containing a disconnection dipole. (a) Example of MSD versus time curves for diffusive displacements of Al and Si atoms parallel to the disconnection lines (Y -axis). The three curves for each chemical element correspond to the temperatures of 630 K, 640 K and 650 K in the order of increasing diffusion coefficients. (b) Disconnection diffusion is accompanied by occasional injection of displacement cascades into the Al lattice which often return to the disconnection core (1 ns time interval shown). (c) The net displacement field in the interface plane over the time interval of 8 ns indicates fast diffusion along disconnection lines. In (b) and (c), atomic displacements are colored by atomic type with Si displacements shown in blue and Al displacements in red.

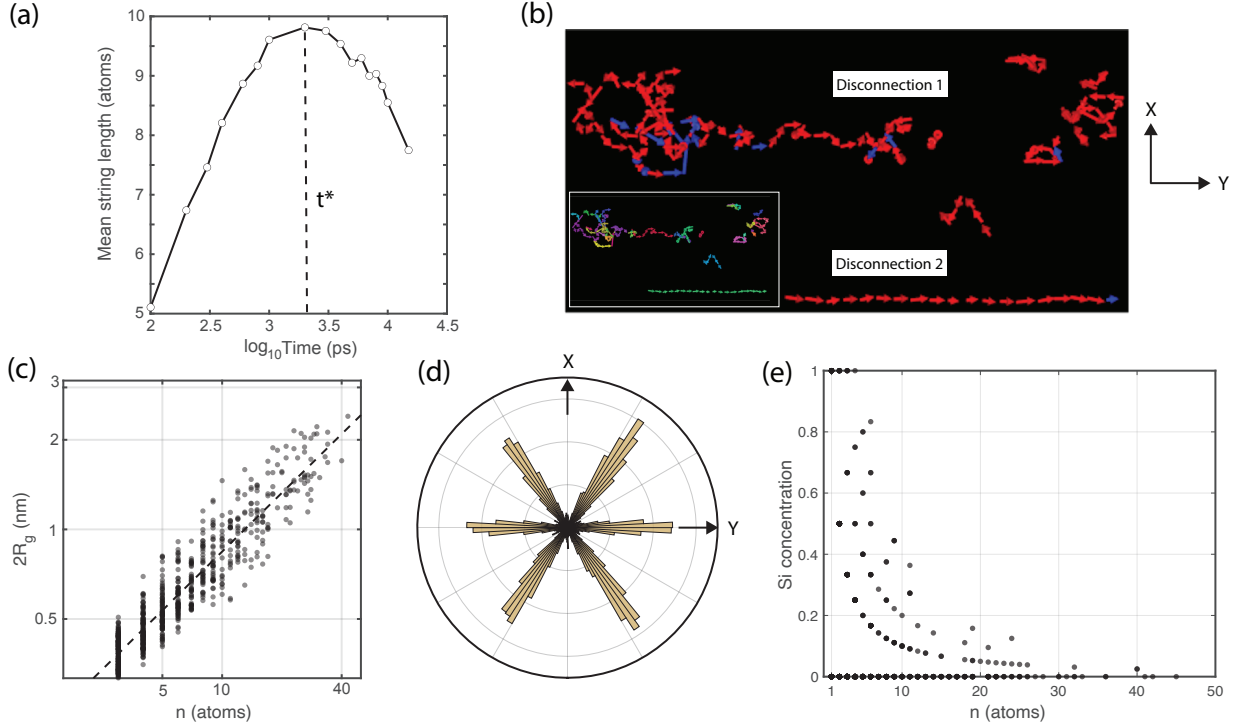


Figure 5: Collective diffusion mechanisms in Al-Si interphase boundaries. Diffusion along the interphase boundary disconnections exhibits hallmarks of dynamic heterogeneity, such as: (a) Characteristic timescale t^* associated with the formation of mobile string-like atomic clusters. The mean string contains about 9 atoms for top 50% of mobile atoms. (b) Examples of strings for the time interval of t^* with string-like displacements colored by atom type (blue = Si, red = Al). The string-like clustering is shown in the inset with different colors representing different clusters. (c) The fractal dimension of $d = 1.5$ of string-like clusters was extracted from the linear fit (dashed line) of the gyration radius R_g versus string size n in logarithmic coordinates. (d) Stereographic histogram of atomic displacement directions reveals a propensity for the motion in the close-packed $\langle 110 \rangle$ directions. (e) Si concentration (atomic fraction) in the strings plotted as a function of string size. Si atoms play a lesser role in the collective diffusion mechanisms than Al atoms but still participate in the collective diffusion events.

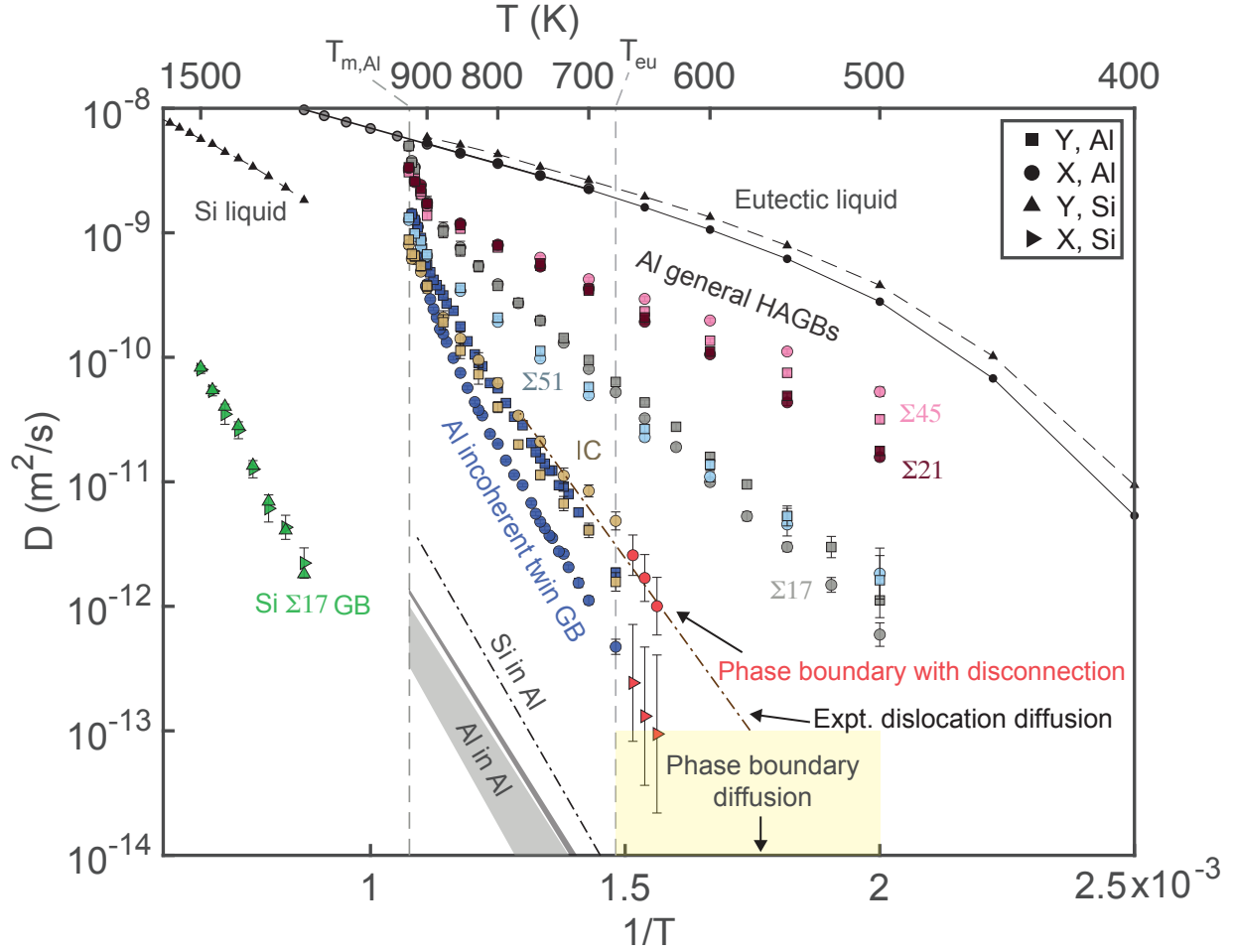


Figure 6: Arrhenius diagram of diffusion in Al, Si, and Al-Si systems. The yellow box indicates the estimated range of diffusivity in planar or faceted Al-Si interphase boundaries without extrinsic defects. The Al-Si interface containing disconnections (red symbols) exhibits Al diffusion rates lower than those for general high-angle GBs (HAGBs) and similar to those for the incommensurate (IC) and incoherent twin GBs. Many GBs exhibit anisotropic diffusion in the X and Y directions. Experimental data is shown for lattice diffusion (Al in Al, Si in Al) and Si diffusion along Al dislocations (dash-dotted line).

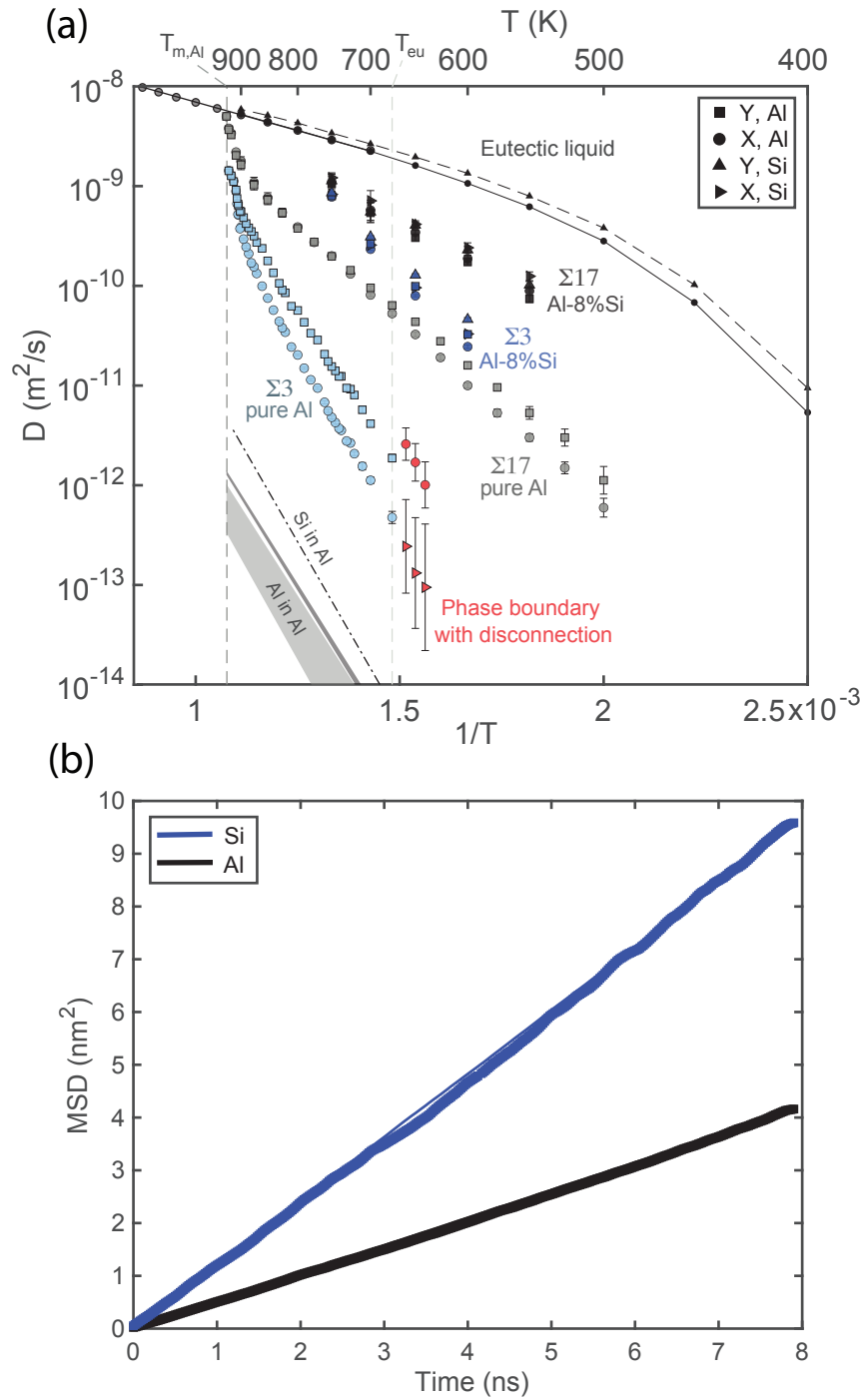


Figure 7: (a) Arrhenius diagram of Al and Si diffusion in the Si-enriched $\Sigma 3$ and $\Sigma 17$ GBs in Al-8at.%Si alloy. Selected data from Fig. 6 is included for comparison. (b) Example of MSD versus time curves along the tilt axis of the $\Sigma 3$ incoherent twin GB at 650 K. The lines represent linear fits. The plots demonstrate that Si atoms diffuse in GBs faster than Al atoms.

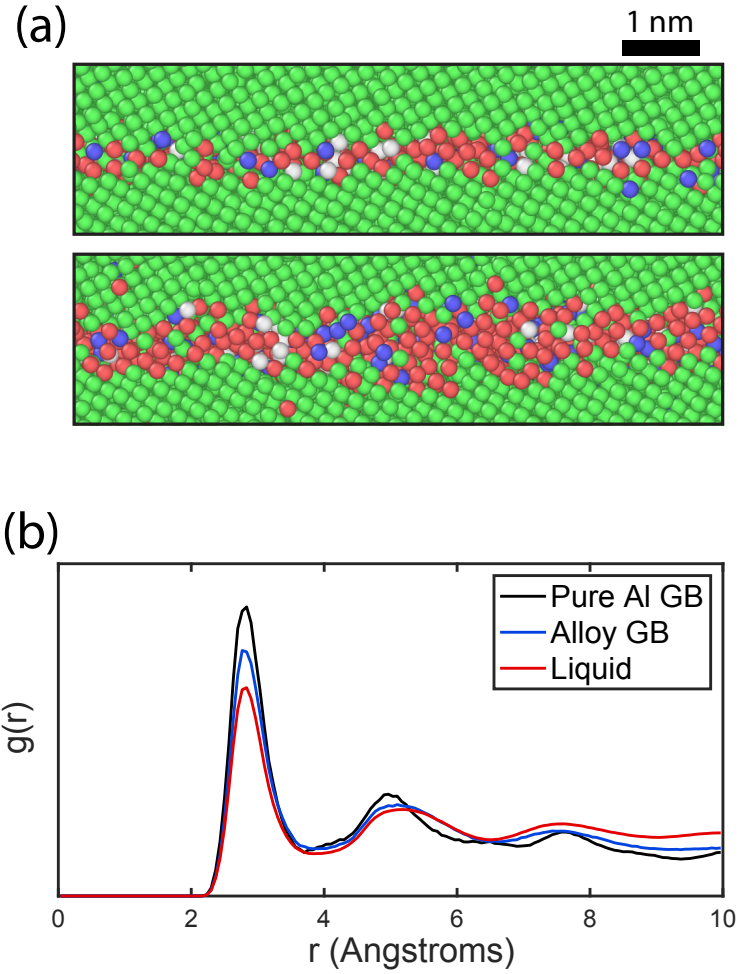
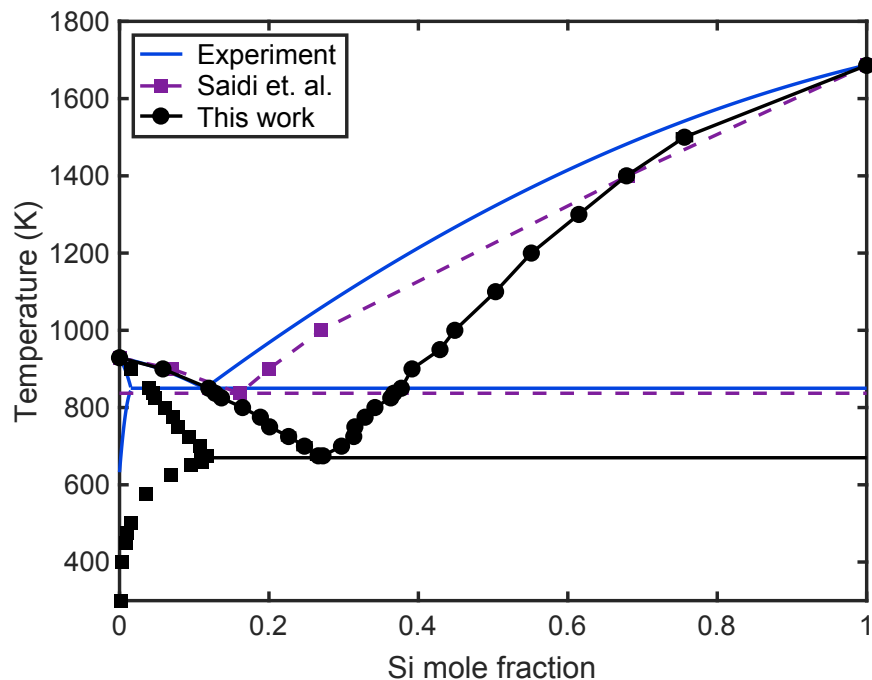


Figure 8: GB structures in Al-Si alloys at the temperature of 750 K. (a) $\Sigma 17$ GB in pure Al (top panel) and Al-8at.%Si alloy (bottom panel). The atoms are colored by local coordination: green = FCC, blue = DC, and all other colors represent atoms in locally disordered environments. (b) Radial distribution function of Al atoms in the core of the pure Al GB, the alloy GB, and in supercooled eutectic liquid. The plot demonstrates that the alloy GB is in intermediate state of order between the Al GB and bulk liquid.

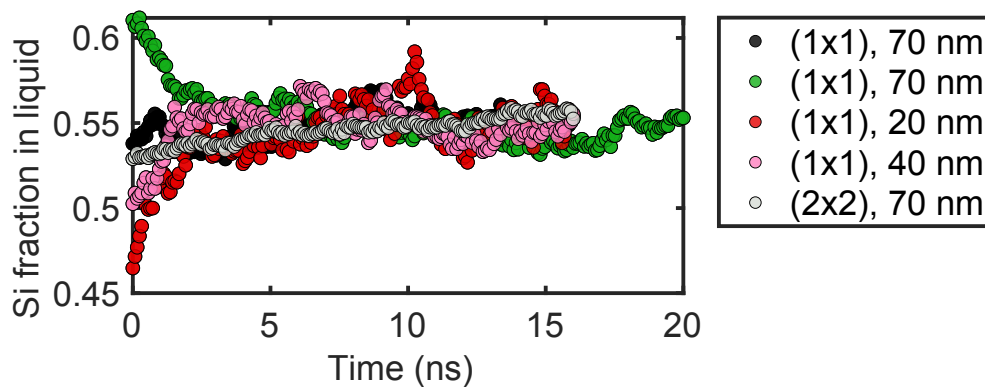
Supplementary Information

GB description	X	Y	Z	γ (mJ/m ²)
$\Sigma 3$ $\langle 110 \rangle$ tilt 70.5°	$[-1, 1, 1]$ $[1, -1, -1]$	$[0, 1, -1]$ $[0, -1, 1]$	$[2, 1, 1]$ $[2, 1, 1]$	418
Al(110) Al(100)	$[0, 0, 1]$ $[1, 1, 0]$	$[1, -1, 0]$ $[-1, 1, 0]$	$[1, 1, 0]$ $[0, 0, 1]$	389
$\Sigma 51$ $\langle 551 \rangle$ tilt 180°	$[5, -5, 1]$ $[5, 5, -1]$	$[8, 9, 5]$ $[-8, 9, 5]$	$[-2, -1, 5]$ $[2, -1, 5]$	498
$\Sigma 17$ $\langle 100 \rangle$ tilt 61.9°	$[5, -3, 0]$ $[-5, 3, 0]$	$[0, 0, -1]$ $[0, 0, 1]$	$[3, 5, 0]$ $[3, 5, 0]$	488
$\Sigma 21$ $\langle 531 \rangle$ asymmetric tilt 80.4°	$[10, 1, -5]$ $[5, -3, -1]$	$[1, 5, 3]$ $[2, 3, 1]$	$[4, -5, 7]$ $[0, -1, 3]$	569
$\Sigma 45$ $\langle 851 \rangle$ tilt 180°	$[11, 2, 1]$ $[11, -2, 1]$	$[-1, 8, -5]$ $[1, 8, 5]$	$[-1, 3, 5]$ $[-1, -3, 5]$	593

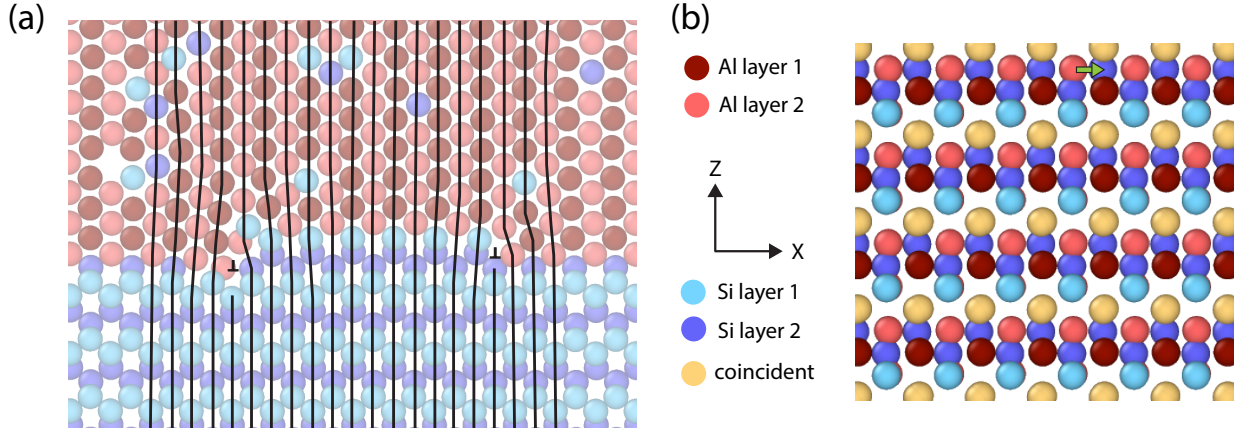
Supplementary Table 1: Crystallography and 0 K energies of Al GBs studied in this work. The Cartesian X , Y and Z axes are aligned with edges of the rectangular simulation box. The GB plane is normal to the Z -direction. For each GB, the two lines indicate crystallographic directions parallel to the Cartesian axes in the upper and lower grains. The 0 K GB energy (γ) was computed with the interatomic potential from Ref. [85]. The data is sorted based on the magnitude of the diffusion coefficient at 700 K from lowest to highest.



Supplementary Figure 1: Al-Si phase diagram computed in this work in comparison with the experimental diagram [53] and previous calculations by Saidi et al. [42].



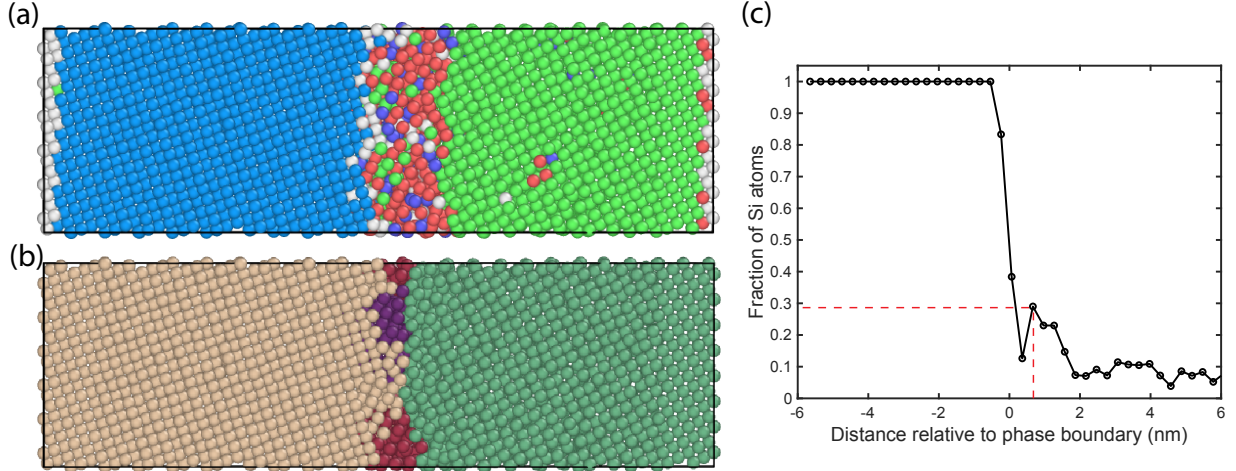
Supplementary Figure 2: Examples of a convergence checks for MC-MD calculations of the Al-Si phase diagram. Data is shown for an example point on the liquidus line on the Si-rich side of the diagram for multiple initial Si concentrations in the liquid and multiple solid-liquid interface cross-section sizes. In the legend, (1x1) refers to the integer repeats of a 1.2 nm x 1.2 nm interface cross section, while the second number is the thickness for the liquid and solid layers.



Supplementary Figure 3: Characterization of phase boundary disconnections. (a) The $\{110\}_{\text{Al}} \parallel \{001\}_{\text{Si}}$ interface structure with the same color coding as in Fig. 3a of the main text. Vertical atomic rows in coherent regions are outlined to reveal the dislocation content of the interface localized near the terminated atomic planes. (b) Coherent dichromatic pattern of the same interface obtained by appropriate straining of the Al phase. The green arrow indicates the disconnection Burgers vector, whose indices are $1/2 \langle 100 \rangle$ relative to the Al lattice and $1/2 \langle 110 \rangle$ relative to the Si lattice.

Further study of interface-induced recrystallization

Al recrystallization induced by the Al-Si interphase boundary starts with a transient state in which a Si-enriched layer forms on the Al side of the interface. This layer can be interpreted as a nucleus of a new Al grain separated from the parent grain by a GB containing some amount of segregated Si. How far this GB migrates into the parent grain depends on whether a sufficiently large thermodynamic force exists for GB migration. We hypothesize that, in our simulations, the driving force is an elastic strain energy difference across the GB which arises due to the lattice misfit at the Al-Si interface. A large strain energy difference can drive the growth of the new grain deep into the old. If, by crystal symmetry, there is no elastic energy difference across the GB, as in the case of symmetric tilt GBs, or if the misfit strain energy density is too small, then the driving force will be insufficient to cause significant GB migration. The recrystallization will then result in a narrow splitting of the initial interface into one with a more stable crystallographic orientation and a thin layer representing a new Al grain parallel to the interface. The latter scenario is illustrated in Fig. 4, where the recrystallization does not proceed beyond creating a Si-enriched GB on the Al side.

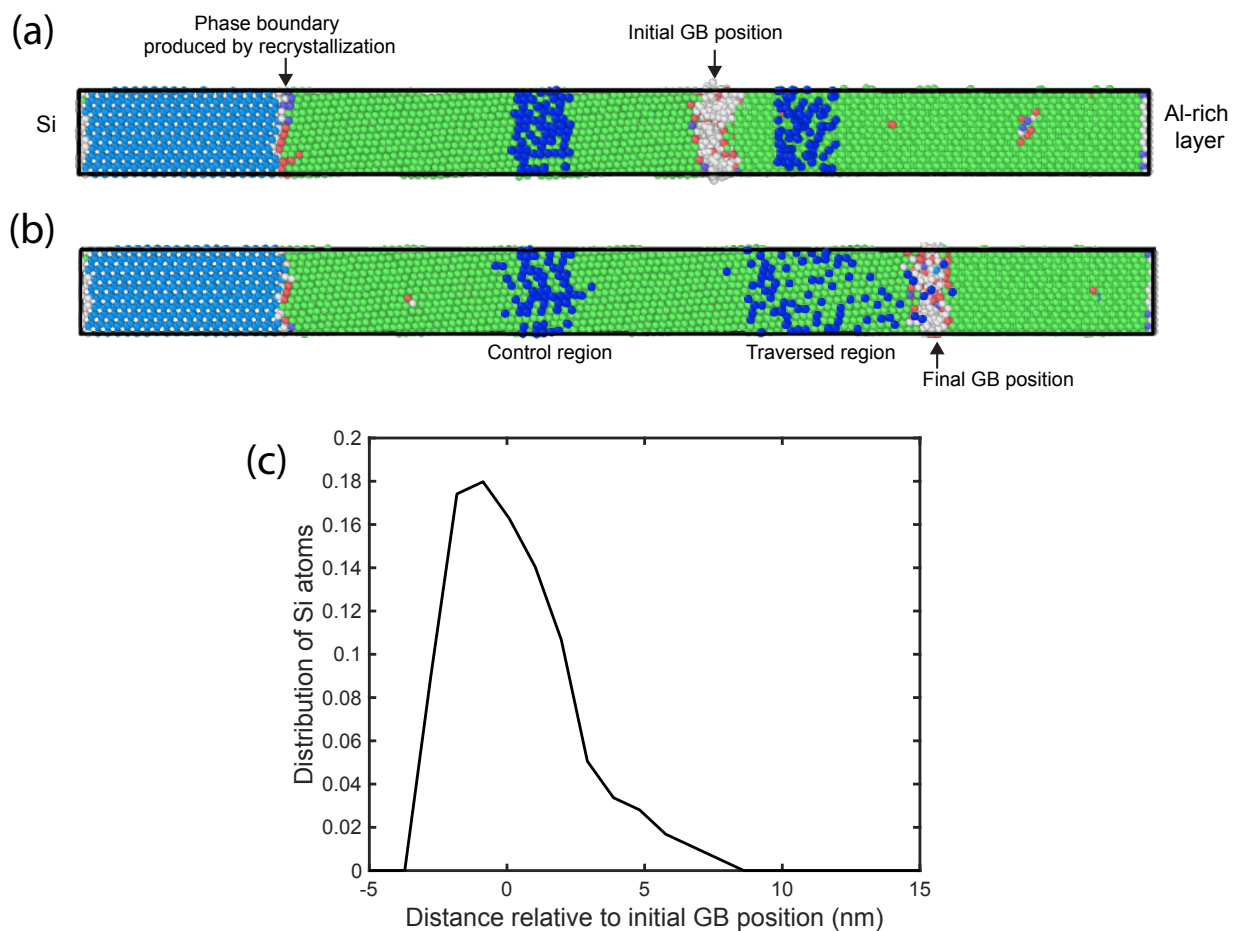


Supplementary Figure 4: Example of interface-induced recrystallization without GB migration. The initial interphase boundary has the same crystallography as a $\Sigma 5$ (210) $\langle 100 \rangle$ tilt GB. (a) After an MC/MD anneal, the interface develops a Si-enriched, partially disordered layer on the Al side. (b) Spontaneous formation and dissolution of subcritical nuclei of new grains is revealed by grain segmentation analysis (distinct grains have different colors). (c) The Si concentration peak with a near eutectic composition (dashed lines) can be interpreted as a new GB with Si segregation. This splitting of the interface structure represents an embryonic form of interface-induced recrystallization.

When the recrystallization triggers a significant GB migration, the process is accompanied by a solute drag. In the example shown in Fig. 5, the crystallographic orientation across the interphase boundary is the same as in Fig. 4 but the interface cross-section is relatively small and the lattice misfit is large (4%), creating a large strain energy differential across the GB. Fig. 5 demonstrates the drag of Si atoms by the moving GB using the technique proposed in [86]. Si atoms were colored for tracking purposes in two stripes parallel to the interface: one stripe was chosen ahead of the moving GB and the other (control stripe) behind the GB. As the GB traverses the right-hand stripe during the motion, it scatters the Si atoms due to the accelerated (“short circuit”) GB diffusion as well as by dragging the Si atoms in the direction of motion. The diffusion-induced scattering alone would cause a nearly even spreading of the Si composition profile in both directions. By contrast, the solute drag spreads the solute atoms predominantly in the direction of GB motion, creating a long tail in the composition profile. This tail was clearly observed in our simulations (Fig. 5c), providing evidence that the Si atoms were indeed dragged by the GB.

The previous direct observation of solute drag by MD simulations was possible due to slow migration velocities ranging between 0.01 and 0.1 m/s [86]. Here, we observed the solute drag at surprisingly large GB velocities of ≈ 1 m/s. The stronger solute drag in the Al-Si system likely originates from the relatively fast Si diffusion in Al and the highly

disordered GB structure that easily absorbs Si atoms.



Supplementary Figure 5: Solute drag during GB motion caused by interface-induced recrystallization. (a) Si atoms in two stripes behind and in front of the moving GB are colored in blue for tracking. (b) The GB scatters the Si atoms in the stripe traversed by the GB migration, providing evidence of Si drag by the moving GB. (c) The solute drag is further confirmed by the long tail in the Si composition profile after the right-hand stripe was overrun by the GB.